Inelastic rotations and pseudoturbulent plastic avalanches in crystals

R. Baggio [1,2,3] O. U. Salman [1] and L. Truskinovsky[2]

[1]*LSPM, CNRS UPR3407, Paris Nord Sorbonne Université, 93400 Villateneuse, France*
[2]*PMMH, CNRS UMR 7636 ESPCI ParisTech, 10 Rue Vauquelin,75005 Paris, France*
[3]*UMR SPE 6134, Université de Corse, CNRS, Campus Grimaldi, 20250 Corte, France*

Plastic deformations in crystals produce microstructures with randomly oriented patches of unstressed lattice forming complex textures. We use a mesoscopic Landau-type tensorial model of crystal plasticity to show that in such textures rotations can originate from crystallographically exact microslips which self organize in the form of laminates of a pseudotwin type. The formation of such laminates can be viewed as an effective internal "wrinkling" of the crystal lattice. While such "wrinkling" disguises itself as an elastically neutral rotation, behind it is inherently dissipative, dislocation-mediated process. Our numerical experiments reveal pseudoturbulent effective rotations with power-law distributed spatial correlations which suggests that the process of dislocational self-organization is inherently unstable and points toward the necessity of a probabilistic description of crystal plasticity.

I. INTRODUCTION

The emerging experimental evidence of intermittent avalanches and scale-free dislocation patterns triggered a shift from macro- to microscale modeling efforts in crystal plasticity [1–3]. The recorded temporal and spatial correlations were interpreted as evidence of complex cooperative dynamics at subcontinuum scales [4–6]. Most strikingly, the observed hierarchically organized deformation fields were likened to scale-free turbulent flows [7–12]. Since fluid turbulence largely relies on vortices, the question arises whether large rotations play a similarly crucial role in crystal plasticity [13–17].

A. Inelastic rotations

When crystalline specimens are deformed plastically, both elastic and inelastic rotations are revealed through the emergence of deformation-induced crystallographic textures. They have been understood as a strain-accommodation strategy, allowing the crystal to ensure lattice compatibility without accumulation of considerable elastic stresses [18,19]. Energetically neutral rotations are also behind the localization of dislocations in wall structures which separate misorientated lattice patches [20–25]. While the formulation of an adequate description of texture development is commonly recognized as one of the most challenging tasks for theories of crystal plasticity, the microscopic mechanisms of particularly large rotations involved in textures formation remain obscure [18,19,26–30].

Plastic rotations in crystals mainly occur by slip, however other dislocation mediated modes of inelastic deformation may also contribute to changes in crystallographic texture [22,31–33]. Thus, recent molecular dynamic simulations of single-crystal plasticity suggested that, at least in the case of the discontinuous yield of defect-free crystals, the patchy local reorientation of the crystal lattice is due to deformation-induced micro- or nano-twinning [34–38]; in physical experiments similar effects were as well observed [39,40]. In this paper, we corroborate the idea of large inelastic rotations by microtwinning theoretically while emphasizing the point that such twinning ultimately relies on dislocation glide. More specifically, we conduct numerical experiments showing explicitly how crystallographically specific inelastic deformations of twinning type can disguise themselves as large crystal rotations.

B. Previous work

Considerable efforts have been recently devoted to the task of small-scale modeling of crystal plasticity at a reasonable computational cost. A fully detailed description of plastic flows in crystals is possible only by molecular dynamics (MD) or molecular statics (MS) approaches [41–43], which accurately represent micromechanisms of plastic response while relying minimally on phenomenology. However, in most applications, such an approach is prohibitively computationally expensive, even if one deals with ultrashort timescales and ultrasmall samples. Partial averaging of atomistic MD has emerged in the form of a continuum phase-field crystal method (PFC) [44,45]; however, the resulting microscopically detailed description of lattices still remains too demanding in terms of computer time, at least in the case of developed plastic flows with a realistic number of interacting dislocations.

The discrete dislocation dynamics (DDD) approach was created to overcome the short-scale focus of atomistic methods and inform various classical continuum models. The DDD modeling is very powerful, allowing one, for instance, to

model the organization of dislocations into cell structures [46–48]. However, the DDD models contain many parameters since the processes of dislocation nucleation, interaction with defects, self-locking, climbing, etc., have to be prescribed phenomenologically through specific local rules coming from independent phenomenological constructs. Other major challenges in the DDD framework include accounting for large plastic distortions and incorporating the effects of anisotropic elasticity [49]. Coarse graining of DDD has been attempted in the mesoscopic stochastic continuum dislocation dynamics (CDD) where dislocation microstructures are modeled by various continuum dislocation density fields [50]. While various phenomenological closure relations have been proposed to model the evolution of such fields, the systematic development of this approach is hindered by the fact that rigorous statistical averaging in the ensemble of strongly interacting dynamic defects is still a tough challenge [51–53].

In search of a micro-macro compromise, a multiscale quasicontinuum (QC) approach was developed based on the observation that a fully atomistic resolution is necessary only in small spatial regions, while in the rest of the computational domain, where the deformation fields change slowly, the classical continuum theory can be still used [54]. The necessity of patching the continuum and discrete subdomains poses, however, a complex problem. Also, the necessity to resolve all the scales fully adequately makes this method hardly applicable to the description of collective dislocation processes.

A powerful mesoscale approach to crystal plasticity, which involves averaging over small scales and therefore allows one to treat dislocations in a continuum framework, is the phase field dislocation dynamics (PFDD) [55,56]. In this approach, lattice slips are described by scalar order parameters, while the energy wells correspond to lattice invariant shears. The main problem of this approach is that lattice invariant shears are resolved by scalar order parameters only approximately even if PFDD is extended to finite strains [57].

C. Mesoscopic tensorial model

All these computational platforms are successful in addressing particular time and length scales, with higher-scale models (more coarse-grained) relying on input from lower-scale models (less coarse-grained). However, as we have seen above, each one of them has its limitations.

To achieve a compromise between more and less coarse-grained models we adopt in our numerical experiments an approach [58,59] which is both versatile and synthetic in the above sense. Known as the mesoscopic tensorial model (MTM), it represents a crystal as a collection of homogeneously deforming elastic elements whose nonlinear elastic response is governed by globally periodic potential defined in the space of metric tensors. The potential is designed to respect the geometrically nonlinear kinematics of the lattice, as originally envisioned in Refs. [60–67]. From the perspective of the ensuing Landau-type model, the potential has an infinite number of equivalent energy wells, and therefore plastically deformed crystals can be viewed as coherent mixtures of equivalent "phases" [59,68].

To follow the response of the system one can use the real physical space or the configurational space of metric tensors where individual mesoscopic elements are represented by configurational points. As long as the affine configuration remains stable, the points, representing different elastic elements in the configurational space are all superimposed and follow together the prescribed loading path. After the instability, the configurational points spread around the configuration space with different equivalent energy wells getting unequally populated. During such configurational spreading the crystal is deforming plastically as the elastic energy is lost irreversibly. In particular, plastic yield of a pristine crystal can be interpreted as a massive escape of the configurational points from the reference energy well while plastic "mechanisms" can be linked to the configuirational "flows" along low-barrier valleys in the energy landscape. Friction-type dissipation, controlling dynamics in continuum crystal plasticity, emerges in such a theory as a result of a homogenized description of overdamped athermal dynamics in a rugged energy landscape which takes the form of a succession of the discontinuous branch switching events [69].

The MTM-based computational approach to crystal plasticity bears some resemblance to the local version of the quasicontinuum model [70–72] and also has features in common with tensorial generalizations of phase-field approaches to dislocational plasticity [57,73–76]. Its main advantage is the geometrically adequate account for both large strains and large rotations. Another important benefit is the possibility to model both short and long-range interactions of dislocations without any macroscopic phenomenological assumptions. For instance, dislocation nucleation, dislocation annihilation, and dislocation locking emerge naturally from this modeling framework, moreover no ad-hoc rules are needed for specifying the activated slip planes.

We reiterate that the most important assumption behind MTM is that the crystal admits a pseudocontinuum strain energy density whose invariance is dictated by the global symmetry group of simple lattices, known as $GL(3, \mathbb{Z})$ [77]. From this point of view, the MTM can be considered as a multidimensional, finite-strain generalization of the Peierls-Nabarro [78,79] and Frenkel-Kontorova [80] one-dimensional models which also operate with globally periodic energies. However, in contrast to these purely prototypical models, the MTM potentials, constructed using *ab initio* methods, allow one to make fully quantitative predictions for crystals with particular crystallographic symmetries.

D. Benchmark test

As a proof of principle, we develop in this paper a MTM description of a single plastic avalanche resulting from a brittle-like yield of a homogeneously deformed pristine crystal. Our study was inspired by the recent fully atomistic simulations of bulk single-crystal plasticity in the uniaxially compressed body-centered cubic metal tantalum [34]. In the reported numerical experiments a defect-free, perfect crystal yielded discontinuously after reaching critical stress. Analysis of crystal configurations attained under strain revealed that the perfect metal yielded largely by deformation twinning—that is, by sudden strain-induced reorientation of the crystal lattice within bounded volumes of the material. To rationalize these

observations we conducted our own numerical experiments using the MTM approach.

In our numerical experiments we used quasistatic hard loading device (strain-controlled) and the response was obtained by incremental minimization of the total energy of the collection of coupled elastic elements. As we have already mentioned in such apparently pseudoelastic approach the energy dissipation is taking place during discontinuous branch switching events [69]. In the language of crystal plasticity the branch switching can be associated with dislocation avalanches which involve collective nucleation, annihilation, and reorganization of dislocations.

If a pristine crystal is loaded quasistatically, the very first avalanche of this type, signaling the catastrophic, brittle-like transition from affine to nonaffine configuration, takes the form of a massive system-size dislocation nucleation. As we show, during such an event, multiple dislocations appear collectively while the lattice rearranges itself into almost fully relaxed domains (or patches) with different orientations. Our numerical experiments provide a compelling evidence that in most of such domains, the apparent rigid rotations are achieved through coordinated, spatially distributed lattice invariant shears, resulting in the formation of highly specific microtwinned laminates.

The importance of energy-minimizing macroscale laminates has been already realized in continuum crystal plasticity [81,82]. In such macroscopic framework lamination was shown to result from the nonconvexity of the effective energy functional induced by geometric softening and/or latent hardening. Here we focus on the consequences of the microscopic energy nonconvexity associated with the presence of lattice invariant shears. We show that it can indeed lead to the formation of crystallographically specific laminates at the microscale. Moreover, we provide a compelling evidence that the corresponding oscillatory bandlike microstructures (representing alternating crystal orientations), can be interpreted as microtwinning.

E. Main results

In contrast to physical experiments, the MTM modeling allows one to track the deformation history of individual elastic elements. Using this capability of MTM, we were able to trace how exactly the microtwin laminate form and how they self-organize to present themselves macroscopically as pseudorigid rotations. The dissipative, dislocation-mediated nature of such self-organization suggests that at least some of the macroscale textures, sometimes naively associated with purely elastic or even rigid rotations, emerge from the collective motion of dislocations. Using MTM we could study the transient process of avalanche unfolding in full detail and show that the modulated structure of a microtwin results from the propagation of an interface between the unstable homogeneous configuration and the stable oscillatory configuration.

Furthermore, our numerical experiments focused on transient dynamics revealed that the formation of disoriented patches of the unstressed lattice during discontinuous avalanches is inherently unstable even though the sizes and the misorientations of the individual patches end up being highly correlated. The quantitative statistical analysis of the emerging spatial correlations suggests that the underlying process of dislocational self-organization indeed resembles fluid turbulence. All this points toward the necessity of a probabilistic description of crystal plasticity, at least if the study of plastic fluctuations is at stake.

F. Organization of the paper

The rest of the paper is structured as follows. In Sec. II we formulate the MTM approach, and introduce the atomistically informed energy density accounting for the global symmetry of a square lattice. The numerical set up and the outcomes of our numerical experiments are presented in Sec. III. In Sec. IV we reveal the mechanism of rigid rotations recorded in our numerical experiments and link them to microtwinning. In Sec. V we present the analysis of the two simplified models whose aim is to elucidate in the most transparent form the kinetic mechanism of dislocation driven microtwinning disguised as rotation. The pseudoturbulent analogy is discussed in Sec. VI. Finally, in the last Sec. VII we summarize the results and present our conclusions.

II. THE MODEL

In this paper we limit our analysis to the simplest nontrivial 2D problem while assuming that a model crystal can be represented by a collection of $N \times N$ mesoscopic triangular discrete elements organized in a square lattice filling the macroscopic domain Ω_0. The internal scale of order N^{-1} is then viewed as a physical parameter defining the (Kolmogorov-type) cutoff beyond which the deformation is considered homogeneous. To describe the deformation of discrete elements we introduce the piecewise smooth mapping $\mathbf{y} = \mathbf{y}(\mathbf{x})$, where $\mathbf{y}$ are their actual and $\mathbf{x}$ their reference coordinates. We then associate with each element an elastic energy density ϕ which depends on the metric tensor $\mathbf{C} = \mathbf{F}^T \mathbf{F}$, where $\mathbf{F} = \nabla \mathbf{y}$ is the deformation gradient.

A. Configurational space

All deformations that map a Bravais lattice into itself will be accounted of if we require that $\phi(\mathbf{C}) = \phi(\mathbf{m}^T \mathbf{C} \mathbf{m})$ for any $\mathbf{m}$ from an infinite discrete group $GL(2, \mathbb{Z}) = \{\mathbf{m}, m_{IJ} \in \mathbb{Z}, \det(\mathbf{m}) = \pm 1\}$. To explain why such group must indeed include all invertible matrices with integral entries and determinant ± 1, we need to recall that each 2D simple (Bravais) lattice is described by two linearly independent vectors $\{\mathbf{e}_I\}$, $I = 1, 2$, representing the lattice basis. Infinite number of basis vectors exist describing the same lattice structure; two bases $\mathbf{e}_I^0$ and $\bar{\mathbf{e}}_I$ corresponding to the same lattice are related through $\mathbf{e}_J^0 = m_{IJ}\bar{\mathbf{e}}_I$ with $m_{IJ} \in \mathbb{Z}$ a unimodular matrix with integer entries. Therefore, it is exactly the symmetry group $GL(2, \mathbb{Z})$ which accounts for the lattice invariant deformations.

It can be shown [83] that $GL(2, \mathbb{Z})$ constitutes the finite strain extension of the crystallographic point group $P(\mathbf{e}_I)$ which describes material symmetries in classical continuum elasticity [84,85]. In the presence of $GL(2, \mathbb{Z})$ symmetry, the space of metric tensors $\mathbf{C}$ partitions into periodicity domains, each one containing an energy well equivalent to the reference one [62,66]. Therefore, if we know the structure of the energy
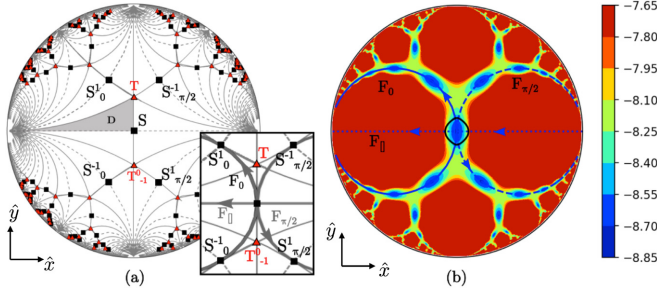
FIG. 1. (a) The configurational space of metric tensors with det $\mathbf{C} = 1$ (Poincaré disk). Infinite families of equivalent square and triangular lattices are shown by squares **S** and triangles **T**, respectively; **D** is the minimal periodicity domain; (b) the energy landscape obtained using an interatomic potential from [87]; a cutoff was applied to improve the visibility of the low-energy valleys. Blue circles: simple shears paths $\mathbf{F}(\alpha, 0)$ (continuous) and $\mathbf{F}(\alpha, \pi/2)$ (dashed). Dotted straight line: pure shear path $\mathbf{F}_{\parallel}(\alpha)$. The dark oval in panel (b) represents the effective yield surface. Coordinate axes are defined in Eq. (1).

FIG. 2. (a) Schematic representation of the triangulated macroscopic domain Ω_0 where the mesoscopic Landau energy is defined on each of the triangles; (b) the atomistic domain Ω_A which represents the response of each of the macroscopic triangles and where the summation in Eq. (2) is performed; here the blue balls represent the actual atoms.

ϕ in one of such domains, then we can use the $GL(2, \mathbb{Z})$ symmetry to find its value in any other point of the configurational space of metric tensors $\mathbf{C}$ described by its three significant components C_{11}, C_{22}, and C_{12}. Since the $GL(2, \mathbb{Z})$ invariance does not concern lattices with different volumes, it is sufficient to focus on the 2D subspace of the configurational space described by the condition $\det \mathbf{C} = C_{22}C_{11} - C_{12}^2 = 1$ [67,86].

To visualize the implied tensorial periodicity of the function $\phi(\mathbf{C})$, it is convenient to stereo-graphically project the hyperbolic surface $\det \mathbf{C} = 1$ on a 2D disk of unit radius (Poincaré disk). In this mapping the point $(\hat{x}, \hat{y})$ on the disk represents the point $((C_{11} - C_{22})/2, C_{12}, (C_{11} + C_{22})/2)$ on the hyperbolic surface with

$$\hat{x} = \frac{\left(\frac{C_{12}}{C_{22}}\right)^2 + \left(\frac{1}{C_{22}}\right)^2 - 1}{\left(\frac{C_{12}}{C_{22}}\right)^2 + \left[\left(\frac{1}{C_{22}}\right) + 1\right]^2}, \hat{y} = \frac{2\left(\frac{C_{12}}{C_{22}}\right)}{\left(\frac{C_{12}}{C_{22}}\right)^2 + \left[\left(\frac{1}{C_{22}}\right) + 1\right]^2}. \quad (1)$$

In such relations, once C_{22} and C_{12} are given, the component C_{11} is determined by the condition $C_{11}C_{22} - C_{12}^2 = 1$.

We illustrate the $GL(2, \mathbb{Z})$-induced tessellation of the configurational surface in Fig. 1(a). The subdomain $D = \{0 < C_{11} \leqslant C_{22}, \quad 0 \leqslant C_{12} \leqslant C_{11}/2\}$, highlighted in gray in Fig. 1(a), contains metric tensors forming the "minimal" periodicity domain. It corresponds to the "minimal" choice for the lattice vectors $\tilde{\mathbf{e}}_1$, $\tilde{\mathbf{e}}_2$, selected according to the algorithm [86]: (step 1) $\tilde{\mathbf{e}}_1$ is the shortest lattice vector; (step 2) $\tilde{\mathbf{e}}_2$ is the shortest lattice vector not colinear with $\tilde{\mathbf{e}}_1$ and for which the sign is chosen in such a way that the angle between the two is acute. The ensuing basis is known as having the "reduced form of Lagrange." It is related to the original basis through the relation $\tilde{\mathbf{e}}_b = m_{ab}\mathbf{e}_a$ from which the matrix $\mathbf{m}$ is identified. The algorithm of Lagrange reduction, can be also recast directly in term of metric tensors $\mathbf{C}$: (step 1) if $C_{12} < 0$, change sign to C_{12}; (step 2) if $C_{22} < C_{11}$, swap the two components; (step 3) if $2C_{12} > C_{11}$ set $C_{12} = C_{12} - C_{11}$ and $C_{22} = C_{22} + C_{11} - 2C_{12}$. For a generic metric $\mathbf{C}$, such
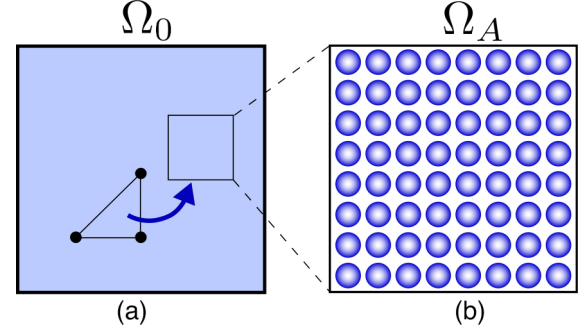
iterative scheme produces the "minimal" equivalent metric $\tilde{\mathbf{C}} \in D$.

Note that in Fig. 1(a) we marked by small black squares the points corresponding to the location of equivalent lattice configurations with square symmetry. The equivalent lattice configuration with hexagonal symmetry (corresponding to triangular lattices) are marked by small red triangles. Simple and centered rectangular lattices form one parametric families and are marked by lines. For the graph theory representation of the relation among equivalent metrics which also reveals additional crystallographic aspects of the underlying energy wells structure, we refer to Refs. [75,88]. It is also instructive to compare the geometrically exact, finite strain, fully tensorial periodicity of the configurational space described above, with an approximate one, generated by theories which rely on linearized strains; see, for instance, Refs. [89–92] and more about it below.

B. Energy landscape

The multiwell (periodic) Landau potential $\phi(\mathbf{C})$ can be computed from a microscale theory using the Cauchy-Born rule [93]. Suppose, for instance, that the atomic interactions are pairwise and that the interatomic potential $V(\mathbf{r}) = V(r)$, where r is the distance between the atoms, is known. Suppose then that material points in a representative volume Ω_A undergo an affine deformation; see Fig. 2. We can write it as $Y_i(X) = X_i + u_i(X)$, where $\mathbf{X}$ and $\mathbf{Y}$ are the coordinates of atoms in the undeformed and deformed states, respectively, and $u_i(X)$ is the displacement vector. The vectors connecting two atoms in the reference configuration are $R_i = X_i - X_i'$ and in the deformed configuration are $r_i = Y_i - Y_i'$. If the deformation is affine, then we can write $r_i = F_{ij}R_j$ where the deformation gradient is $F_{ij} = \partial Y_i/\partial X_j = \delta_{ij} + \partial u_i/\partial X_j$. To compute the energy density $\phi(\mathbf{C})$ we need to account for the deformation of each atomic bond and then average over the domain Ω_A. Given that in the 2D case one can express the interatomic potential in the form

$V(\sqrt{R_1^2 C_{11} + 2 R_1 R_2 C_{12} + R_2^2 C_{22}})$, we can write

$$\phi(\mathbf{C}) = \frac{1}{2\Omega_A} \sum_{\mathbf{X}} \sum_{\mathbf{X'} \in \mathcal{N}(\mathbf{X})} V(\sqrt{R_i C_{ij} R_j}), \qquad (2)$$

where $C_{ij} = F_{ki} F_{kj}$ and the internal summations involves all points $\mathbf{X'}$ belonging to the cutoff neighborhood $\mathcal{N}(\mathbf{X})$. The periodic energy landscape used in subsequent numerical experiments, was constructed using the above algorithm and is based on a particular interatomic potential,

$$V(r) = -2/e^{-8(-1.425+r)^2} - 2/e^{-8(-1+r)^2} + 2/r^{12}, \qquad (3)$$

constructed in Ref. [87] to ensure that the ground state is a square lattice. To perform the sum in Eq. (2), we used the reference square lattice composed of 8×8 atoms with the lattice distance $r_0 = 1.0658$. It is clear that with representative volume Ω_A growing to infinity, the function $\phi(\mathbf{C})$ develops the periodic pattern consistent with the symmetry of lattice invariant shears, e.g., Refs. [94,95]. The choice of the cutoff scale, limiting the volume of volume Ω_A, is dictated in each problem by the required range of (almost) periodicity of the configurational energy landscape. In view of the global symmetry of the energy, it is sufficient to construct the potential $\phi(\mathbf{C})$ using Eq. (2) only inside the minimal periodicity domain D, even if approximately, using a finite rather than an infinite representative volume. Then, as we have seen above, for an arbitrary metric tensor $\mathbf{C}$ one can produce the appropriate symmetry transformation $\mathbf{m}$ and use the mapping $\tilde{\mathbf{C}} = \mathbf{m}^T \mathbf{C} \mathbf{m}$ into D to compute $\phi(\tilde{\mathbf{C}}) = \phi(\mathbf{C})$. The ensuing energy landscape is illustrated in Fig. 1(b).

Note first that as a result of the imposed invariance, energy is periodic along simple shears of the type $\mathbf{F}(\alpha, \theta) = \mathbf{I} + \alpha \mathbf{R}(\theta)\mathbf{e}_1 \otimes \mathbf{R}(\theta)\mathbf{e}_2$, where $\mathbf{e}_i$ is the orthonormal basis of the reference lattice, $\mathbf{R}(\theta)$ is counterclockwise rotation by the angle θ, and α is the magnitude of the shear. In particular, conventional plastic mechanisms for a square lattice correspond to simple shears with $\theta = 0, \pi/2$. Such shears are aligned with the two main close packed crystallographic (slip) planes and therefore correspond to low energy valleys in the configurational landscape shown in Fig. 1(b).

Note also that the loading paths $\mathbf{F}(\alpha, \theta)$ with $\theta = 0, \pi/2$ go through all square wells. In particular, the matrices $\mathbf{F}(\alpha, 0)$ and $\mathbf{F}(\alpha, \pi/2)$ with integer entries mark the bottoms of the equivalent energy wells and correspond to lattice invariant shears. The energy barriers, separating adjacent wells are relatively low which qualifies the corresponding tensorial directions as "soft." On the Poincaré disk such periodically modulated "low-energy valleys" are described by circular trajectories; see Fig. 1(b).

C. Geometrical linearization

Here it is appropriate to remark that the geometrically nonlinear focus of MTM is not redundant and instead has a crucial effect on the outcome of the numerical experiments vis a vis the results obtained in geometrically linearized models [89–92]. Indeed, consider again the two symmetry related shears describing our "soft" loading directions $\mathbf{F}(\alpha, 0)$ and $\mathbf{F}(\alpha, \pi/2)$. In a geometrically linearized description, the com-

ponents of the infinitesimal strain tensor $\boldsymbol{\epsilon} = \frac{1}{2}(\nabla \mathbf{u}^T + \nabla \mathbf{u})$ are the same for both paths:

$$\boldsymbol{\epsilon} = \frac{1}{2}\begin{bmatrix} 0 & \alpha \\ \alpha & 0 \end{bmatrix}. \qquad (4)$$

Instead, in the geometrically nonlinear theory these two configurational directions are energetically equivalent but different. For instance, the associated nonlinear strains tensors $\mathbf{E} = \frac{1}{2}(\nabla \mathbf{u}^T + \nabla \mathbf{u} + \nabla \mathbf{u}^T \nabla \mathbf{u}) = (1/2)(\mathbf{C} - \mathbf{I})$ are different at the second order in α:

$$\mathbf{E}_0 = \frac{1}{2}\begin{bmatrix} 0 & \alpha \\ \alpha & \alpha^2 \end{bmatrix}, \quad \mathbf{E}_{\pi/2} = \frac{1}{2}\begin{bmatrix} \alpha^2 & \alpha \\ \alpha & 0 \end{bmatrix}. \qquad (5)$$

Note that the nonlinear terms ($\propto \alpha^2$) appear along the diagonal entries E_{11} and E_{22}, which describe the stretch along the initial lattice vectors $\mathbf{e}_1$ and $\mathbf{e}_2$. In the small strain limit these vectors do not stretch and the constant volume requirement reduces to the condition that the trace of the linearized strain is zero. Therefore, the linearized states of strain are located on the configurational plane $\mathrm{tr}(\mathbf{C}) = 2$, which is tangent to the configurational hyperboloid of the geometrically nonlinear theory $\det \mathbf{C} = 1$ and therefore agrees with it only locally. On this plane the two paths with $\theta = 0, \pi/2$, corresponding physically to the activation of two different slip systems, merge into one and the two geometrically distinct lattice configurations $\mathbf{F}(\alpha = 1, \theta = 0)$ and $\mathbf{F}(\alpha = -1, \theta = \pi/2)$ are represented by a single point. This causes a well known degeneracy in the geometrically linear theory where one cannot distinguish between the two different slip systems and have to make additional phenomenological assumptions to resolve the degeneracy [96].

III. NUMERICAL EXPERIMENTS

In our numerical experiments a pristine crystal was represented by a homogeneous square domain Ω_0 divided (triangularized) into $600 \times 600 \times 2$ elements aligned with coordinate axes. This sample was loaded quasistatically in a hard device by applying on the boundary an incremental affine deformation $\mathbf{F}$ parametrized by a scalar parameter α. The response of the system is represented by the deformation of the elements described by the functions $\mathbf{y}(\mathbf{x}; \alpha)$.

A. Loading path

To ensure that the response is generic, instead of the "soft" loading directions given by $\mathbf{F}(\alpha, \theta)$ with $\theta = 0, \pi/2$, we used the "hard" loading path corresponding to pure shear

$$\mathbf{F}_{[]}(\alpha) = \begin{bmatrix} \cosh\left(\frac{\alpha}{2}\right) - \sinh\left(\frac{\alpha}{2}\right) & 0 \\ 0 & \cosh\left(\frac{\alpha}{2}\right) + \sinh\left(\frac{\alpha}{2}\right) \end{bmatrix}. \qquad (6)$$

The mapping (6) transforms squares into rectangles and we use here a natural parametrization $\alpha = 2\log(\lambda)$, where (λ, λ^{-1}) are the two principal stretches [97]; the corresponding path in the configurational space is shown by the dashed line in Fig. 1(b). At each step of such loading, parametrized by α, we perform incremental energy minimization. Effectively,

we use continuation method and search for a one parametric family of equilibrium configurations.

B. Numerical method

We reiterate that in the numerical code, the reference body Ω_0 was divided into triangular finite elements. Therefore, we traced the response $\mathbf{y}(\mathbf{x}; \alpha)$ through the deformation of the 2D network of discrete nodes. The nodes $\mathbf{x}$ can be identified using integer-valued coordinates ij and with each node we associated a cell defined by the basis vectors $\mathbf{e}_a(\mathbf{x})$, where $a = 1, 2$. We then treated each triangular cell as a finite element with linear shape functions $N_{ij}(\mathbf{x})$. This allowed us to write the discrete displacement field in the form $\mathbf{u}(\mathbf{x}) = \mathbf{u}_{ij} N_{ij}(\mathbf{x})$, where $\mathbf{u}_{ij}$ denote the values of displacement at node ij. The discrete deformation gradient is then $\nabla \mathbf{y} = \mathbf{1} + \mathbf{u}_{ij} \otimes \nabla N_{ij}$.

We recall that the elastic energy of a cell $\phi(\mathbf{C})$ associated with node $\mathbf{x}$, is a function of the metric tensor $\mathbf{C} = \nabla \mathbf{y}^T \nabla \mathbf{y}$. To minimize the energy functional $W = \int_{\Omega_0} \phi d\Omega_0$ we used a variant of conjugate gradient optimization known as the L-BFGS algorithm [98]. It finds solutions of the equilibrium equations $\partial W / \partial \mathbf{u}_{ij} = \int_{\Omega_0} \mathbf{P} \nabla N_{ij} d\Omega_0 = 0$, where $\mathbf{P} = \partial \phi / \partial \nabla \mathbf{y}$, that are reachable through algorithmically defined, effectively overdamped dynamics. In view of the hard device loading, the positions of surface nodes were set to satisfy $\mathbf{y} = \mathbf{F}_{\parallel}(\alpha) \mathbf{x}$.

The simulations were performed on a fixed computational grid and we did not seek any grid refinement because, due to the particular structure of the nonconvexity of ϕ, our solid system degenerates and behaves mechanically as a liquid in continuum limit [99]. To avoid this unphysical behavior, we interpreted the mesh/grid size $h \sim N^{-1}$ as a regularizing (cutoff) parameter of physical nature.

As we have already mentioned, in physical terms this parameter is the mesoscopic length at which the deformation can be considered homogeneous. It is also a length scale at which the *ab initio* Cauchy-Born energy of a homogeneously deforming elastic element can be considered periodic in the range of strain which captures all the relevant energy wells.

C. Stress-strain response

In Fig. 3, we present the numerically generated quasistatic stress-strain response of a perfect crystal loaded in a hard device along the path $\mathbf{F}_{\parallel}(\alpha)$. We observe that first the crystal deforms elastically as the affine mapping $\mathbf{F}_{\parallel}(\alpha)$ simply transforms squares into rectangles. The homogeneous elastic branch exhibiting small hardening becomes unstable at $\alpha = \alpha_c$ when the branch switching event (dislocation avalanche) takes place. It is a system size collective dislocation nucleation forcing the stress to drop precipitously to an almost zero level. Such an extreme relaxation of the accumulated elastic stress through a catastrophic avalanche suggests that most of the nucleated dislocations end up topologically compensated and therefore effectively screened. The ensuing defect microstructure is then mostly composed of "statistically stored" (rather than "geometrically necessary") dislocations [100–102].
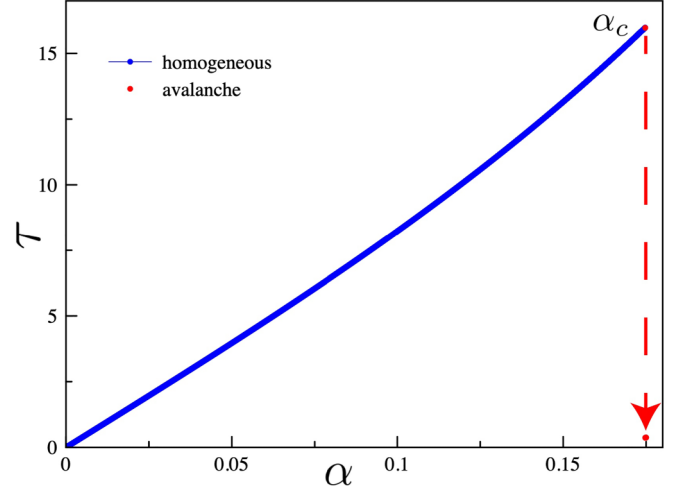

FIG. 3. Quasistatic stress-strain response along the path $\mathbf{F}_{\parallel}(\alpha)$. The stress is projected on the loading direction and averaged over the sample: $\boldsymbol{\tau}(\alpha) = \int_{\Omega_0} \mathbf{P} : (d\mathbf{F}_{\parallel}(\alpha)/d\alpha) d\Omega_0$. The initial nonlinear elastic branch (in blue) corresponds to affine response. The stress drop (in red) corresponds to system size dislocation avalanche at $\alpha = \alpha_c$.

D. Effective yield surface

The value of the critical loading parameter α_c can be anticipated using the macroscopic Legendre-Hadamard (strong ellipticity) criterion [71,103–107]

$$\mathcal{Q}_{ik}(N) = N_J \mathcal{A}_{iJkL} N_L > 0, \tag{7}$$

where the acoustic tensor $\mathcal{Q}_{ik}$, is given by $\mathcal{Q}_{ik} = N_J \mathcal{A}_{iJkL} N_L$, while $\mathbf{N}$ is a vector defined in the Lagrangian (undeformed) configuration. Here $\mathcal{A}_{iJkL}$ is the tensor of elastic moduli:

$$\mathcal{A}_{iJkL} = \frac{\partial^2 \phi}{\partial F_{iJ} \partial F_{kL}}. \tag{8}$$

A rigorous analysis shows that the weak local stability of a homogeneous equilibrium in a hard device is lost when the inequality (7) is no longer strict [108]. At the critical value of the loading parameter the equality emerges in Eq. (7) for some nontrivial $\mathbf{N}$ representing the orientation of the incipient unstable mode.

Note that the instability condition (7) can be also fully projected into the Eulerian space. To this end we need to introduce the Eulerian moduli $\mathsf{a}_{ijkl} = F_{jR} F_{lS} \mathcal{A}_{iRkS}$. The Eulerian version of the acoustic tensor can be then written in the form $q_{ik}(n) = n_j n_k \mathsf{a}_{ijkl}$, which produces the stability criterion:

$$\det[\mathbf{q}(n)] > 0. \tag{9}$$

Applying the condition $\det \mathbf{q} = 0$ to our loading path $\mathbf{F}_{\parallel}(\alpha)$ we verified that the numerically obtained value of the instability threshold $\alpha_c \approx 0.176$ is in excellent agreement with the theoretical prediction.

We similarly applied the condition (9) to a large family of loading trajectories. By interpolating the resulting instability (spinodal) thresholds, we reconstructed the boundary of the affine response, which is illustrated in black in Fig. 1(b). It can be viewed as representing an apparent "yield surface" since an ideal crystal loaded in a hard device will deform
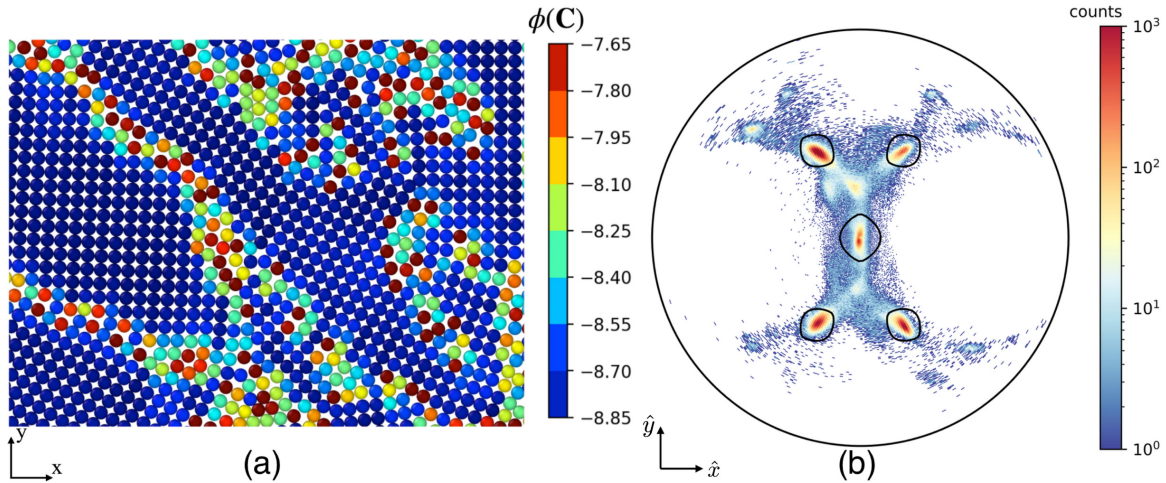
FIG. 4. (a) A fragment of the post-avalanche pattern in real space. The balls represent the nodes of mesoscopic finite elements; colors indicate the level of energy. (b) The distribution of elements in the configurational space for the whole post-avalanche pattern obtained by counting the number of elements inside individual configurational bins. The dark ovals in panel (b) show the effective yield surfaces around the equivalent energy wells (pristine crystal and its four copies obtained by the smallest lattice invariant shears).

homogeneously following the imposed loading path as long as the loading trajectory is contained within such stability region. Note, however, that in a generically loaded inhomogeneous state, the configurational elements can become unstable in a broad area adjacent to this sharp stability boundary, as it is evidenced, for instance, by the studies of dislocation nucleation during highly heterogeneous microindentation tests [109,110].

E. Catastrophic avalanche

We now turn to the description of the system-size instability experienced by a perfect, defectless crystal at $\alpha = \alpha_c$. As we have already mentioned, the breakdown of the affine (elastic) state $\mathbf{y} = \mathbf{F}_0(\alpha)\mathbf{x}$ takes the form of an abrupt drop of both stress and energy, apparently signaling an almost pristine-to pristine transition. In reality, the instability causes the originally homogeneous crystal to rearrange its configuration between the neighboring equivalent energy wells which proceeds through collective generation and self-organization of mutually neutralized dislocations of both signs.

We observe that, as long as the affine configuration remains stable, the points, representing different elastic elements in the configurational space are all superimposed (have the same value of $\mathbf{C}$) and follow together the prescribed loading path. After the instability, the configurational points spread around the configuration space with several equivalent energy wells getting populated. During such configurational spreading the crystal is deforming plastically as the elastic energy is slipping away irreversibly. It is assumed to be lost (dissipated) by either mechanical radiation or through thermalization and eventual heat conduction.

In the physical space, as a result of such catastrophic system-size avalanche, the homogeneously deformed lattice is replaced by a complex texture of variously oriented patches of the unstressed lattice. A fragment of the post-avalanche pattern is shown in Fig 4(a). The balls represent mesoscopic finite elements; colors indicate the level of energy. In Figs. 5(a), 5(b)

and 5(c) we show the snapshots of the evolving element lattice during the avalanche using fast numerical time.

The histogram illustrating the distribution of elements in the configurational space for the whole post-avalanche pattern is shown in Fig. 4(b). It is obtained by counting the number of elements inside individual configurational bins. The dark ovals in Fig. 4(b). show the effective yield surfaces around the equivalent energy wells (original lattice and its four copies obtained by the smallest lattice invariant shears).
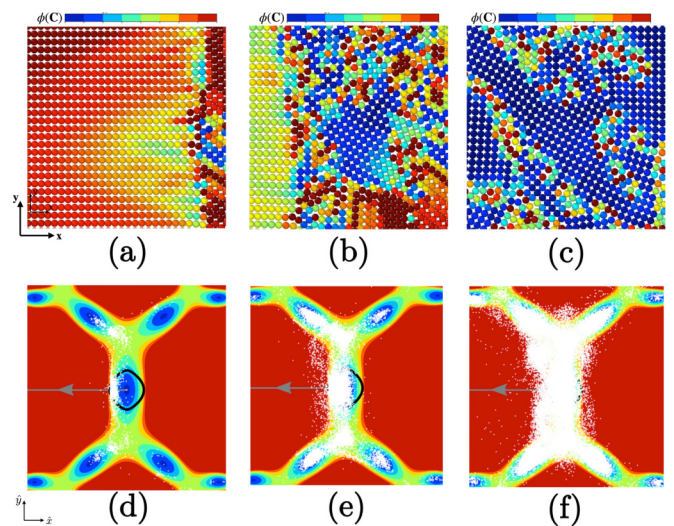

FIG. 5. The unfolding of a dislocation avalanche: [(a)–(c)] in real space (colors indicate the level of strain energy density), [(d)–(f)] in the configurational space of metric tensors. Large red/yellow region in panel (a) corresponds to elastically stressed homogeneous rectangular configuration of the original lattice. Large blue cells in panel (c) correspond to symmetry related versions of unstressed square lattices. White dots in panels [(d)–(f)] show the progressive spreading of the configurational points representing individual elastic elements. The dark ovals show the effective yield surfaces around the energy well corresponding to pristine crystal.

The spreading of the corresponding cloud in configurational space (Poincaré disk) is illustrated in Figs. 5(d), 5(e) and 5(f). In particular, Fig. 5(f) shows the post-avalanche distribution of the deformed elements. One can see that after the instability, most of the homogeneously stretched (rectangular) elements snap back to the reference energy well S. However, a significant percentage of elements also spreads right away over the two symmetric energy wells $\mathbf{S}_1^0 = \mathbf{F}(1, 0)$ and $\mathbf{S}_{-1}^0 = \mathbf{F}(-1, 0)$, which corresponds to the activation of single slip plasticity. The other two symmetric energy wells $\mathbf{S}_1^{\pi/2} = \mathbf{F}(1, \pi/2)$ and $\mathbf{S}_{-1}^{\pi/2} = \mathbf{F}(-1, \pi/2)$ get populated eventually, but only at the end of the avalanche. This indicates that the second main slip system is activated as well. Finally, some elements appear to be locked in the shallow local minima $\mathbf{T}$ and $\mathbf{T}_{-1}^0$ describing the triangular lattice with hexagonal symmetry; such elements appear mostly as the components of Shockley-type partials [111]. The limited occupation by the elastic elements of spaces outside the energy wells reflects the presence of dislocation cores and, more generally, highly heterogeneous defect structures.

We illustrate the gradual unfolding of the system size avalanche in our two movies (presented in the Supplemental Material [112]), which reveal the transient "computational dynamics" hidden behind the apparently discontinuous avalanche. In particular, our movie S1 [112] shows the fast-time evolution of the field $\mathbf{y}(\mathbf{x})$ (coloring shows the level of the nondiagonal component of Cauchy stress, red-high, blue-low). The complementary movie S2 [112] presents the same fast-time evolution but now of the nonaffine component of the field $\mathbf{u}(\mathbf{x}) = \mathbf{y}(\mathbf{x}) - \mathbf{F}_{\parallel}(\alpha_c)\mathbf{x}$ represented by blue arrows.

As we see in these movies, the massive dislocation nucleation starts heterogeneously at the vertical boundaries of the body which play the role of effective lattice defects. It first proceeds in the form of two slowly propagating fronts, originating on these boundaries and separating the remaining affine from the growing nonaffine configuration. Eventually, these fronts get destabilized by the separate nonaffinity originating on the horizontal parts of the boundary which leads to the fast development of considerable spatial complexity. The avalanche ends with another slow stage where the emerging pattern goes through a maturation stage.

Note that if we interpret our "computational dynamics" as a flow of the material, then we may say that as the avalanche unfolds, a relatively "laminar" flow is replaced by distinctly "turbulent" vortex dynamics. However, this spur of activity is only transient and eventually its intensity decays, leaving behind a complex and manifestly multiscale spatial pattern. Similar, correlated nonaffine transient fluctuations during plastic avalanches have been extensively documented in (quasistatic) experiments on granular solids and even interpreted as "granulence"; see, for instance, Refs. [10,113–116]. Turbulent-like displacement fields have been also found to accompany plastic avalanches in amorphous materials. The underlying manifestly non-Gaussian fluctuations have been sometimes associated with a correlated endogenous "noise," e.g., Refs. [117–119]. We discuss the appropriateness of the use of such metaphors for the description of plastic avalanches, observed in our numerical experiments, in Sec. VI.

F. Post avalanche pattern

The detailed post-avalanche pattern in the physical space is shown in Fig. 6(a). Upon magnification we see a complex arrangement of apparently randomly rotated unstressed square lattice patches circumscribed by energy carrying boundaries, see Figs. 6(b)–6(d). A salient feature of this pattern is the ubiquitous presence of the lattice patches rotated at $\pi/2$ with respect to the undeformed reference state; see more about this below. We also see the ubiquitous presence of the fragments of triangular lattice, like the one shown in the inset in Fig. 6, which serve as elements of the stacking fault-type interfaces and also contribute to the structure of at least some dislocation cores. In fact, a detailed study of the deformation of individual elements reveals the presence of both, isolated dislocations and the dislocational-rich extended lattice defects where dislocations interact strongly and their cores may be distorted; see Fig. 7 (1, 2). In particular, the observed high-energy boundaries which separate the extended rotated patches, can be viewed as composed of interacting dislocations locked in stable, wall-type configurations, see Fig. 7 (2). In general, the identification of particular lattice defects and extracting their core structures in mesoscopic computations, where we operate with atomically blurred images, is an even more challenging task than in the case of molecular dynamics [37,120–122]. In this sense our reference to particular lattice defects emerging in mesoscopic simulations can be viewed only as suggestive.

G. Molecular statics

The natural question is then: how realistic is the observed picture? To corroborate the predictions of the MTM-base numerical experiments, we performed a set of parallel molecular statics (MS) simulations employing the same interatomic potential (3). The role of elastic elements in such simulations was played by individual atoms, in other words, we identified for simplicity our regularization length scale with interatomic cut-off distance distance. It is clear that in this case only qualitative agreement between the micro- and mesoscopic pictures can be expected.

In our MS numerical experiments the positions of the atoms for the given boundary conditions were determined by minimizing the energy of a system composed of N_A atoms. It can be written in the form $\Pi = \frac{1}{2} \sum_{\alpha}^{N_A} \sum_{\beta, \beta \neq \alpha}^{N_A} V(r^{\alpha\beta})$, where $r^{\alpha\beta}$ is the distance between the atoms α and β. As we have already mentioned, the interatomic potential $V(r^{\alpha\beta})$ was taken from Eq. (3). The positions of the atoms were found by solving the equilibrium equations $d\Pi/d\mathbf{r}^\lambda = 0$, where $\lambda = 1, \ldots, N_A$. To solve these equations we used the L-BFGS algorithm [98] which builds a positive definite linear approximation of these equations allowing one to make a quasi-Newton step lowering the energy Π. To impose the hard device type boundary conditions we applied affine displacements [of a pure shear type $\mathbf{F}_{\parallel}(\alpha)$] to the atoms within the boundary layer of a small thickness. The amplitude of the loading was incrementally increased and kept fixed during each relaxation step.

As in MTM, in our MS tests the pristine crystal was deforming homogeneously till the critical value of the loading parameter α was reached. At the critical level of strain, which
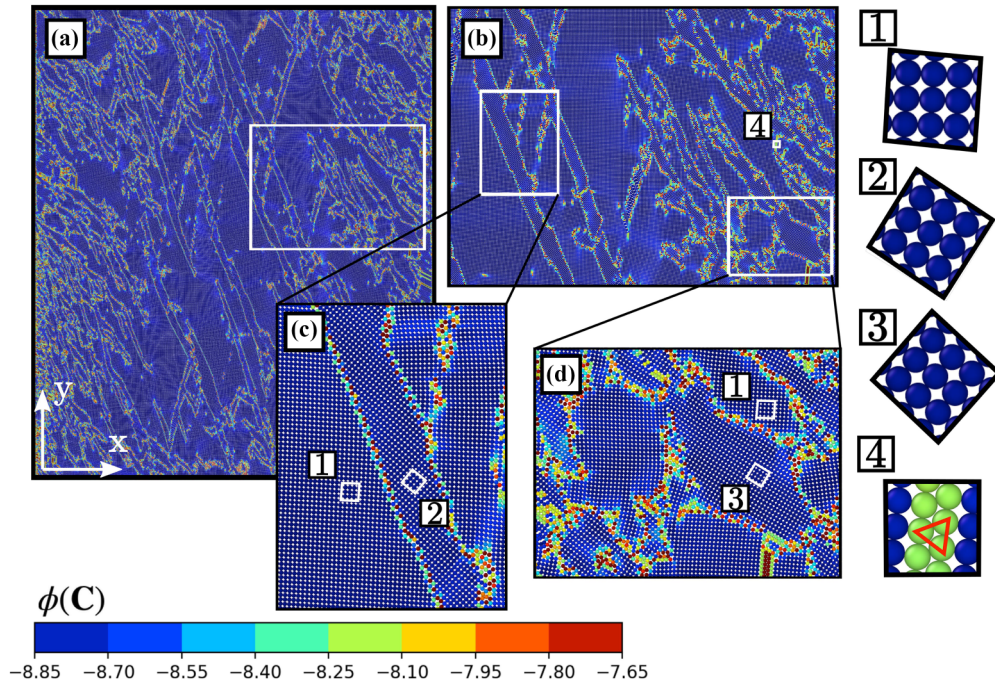
FIG. 6. Post-avalanche pattern shown at different scales. Colors indicate the level of energy. Insets (1–3): relative rotation of unstressed square patches. Inset (4): a fragment of a metastable triangular lattice.

is close to the theoretical prediction, the system size plastic avalanche took place. In Fig. 8, we present a fragment of the post avalanche configuration. It shows the anticipated grain structure. One can see that the misoriented low energy patches of original lattice are practically unloaded. The energy is again localized on the highly dislocated intergrain boundaries. The inset shows a magnified version of the $\pi/2$ rotation of one of the patches relative to the orientation of the original square lattice. Other differently oriented patches are visible as well forming collectively a complex crystallographic texture. The overall picture is similar to the one obtained in our MTM-based experiments which corroborates its basic conclusions. In this paper we do not perform quantitative comparison that would require, in particular, the discussion of the delicate role

of the internal scales in the two models; the corresponding analysis will be presented in a separate paper.

IV. INELASTIC ROTATIONS

In the previous section, we have seen that the MTM approach allows one to trace the emergence of complex multigrain textures and study the formation of the supporting dislocation patterns. In this section, we show that MTM also offers a suitable framework for a deeper theoretical understanding of the observed misorientations angles between the ensuing grains.

The microscopic nature of large rotations in Fig. 6 can be understood if we follow the deformation of the individual elements. Thus, the elemental triangulation of the coexisting patches of types 1–3 in Fig. 6 reveals that an apparent rigid
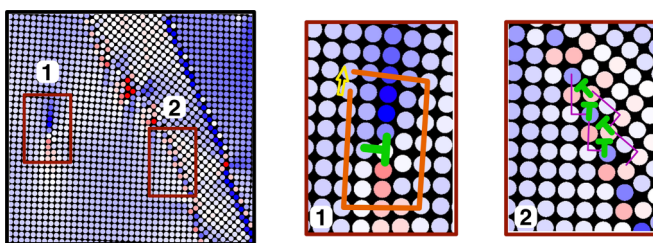

FIG. 7. A fragment of the post-avalanche pattern in physical space extracted from Fig. 6(a); colors indicate the level of the non-diagonal component of Cauchy stress. The zoom into the fragment (1) shows a single dislocation inside a rotated grain; the open circuit around it indicates the corresponding Burgers vector is nonzero with the length equal to the lattice spacing, see the yellow arrow. The zoom into the fragment (2) shows the boundary between the rotated patches whose dislocational structure reveals the $\Sigma 5$ type grain boundary.
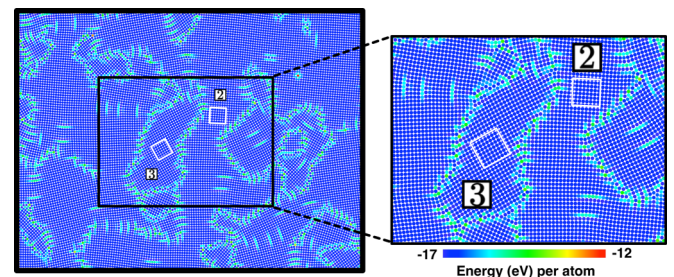

FIG. 8. Final positions of the atoms in our parallel MS study of a system size plastic avalanche showing a fragment of the post-avalanche pattern. Atoms are colored according to the level of their potential energy: red-high, blue-low. The magnification on the right shows an example of an inelastically rotated (microtwinned) domain; numbers have the same meaning as in Fig. 6. Such low-energy domains are separated by high-energy dislocation-rich grain boundaries.
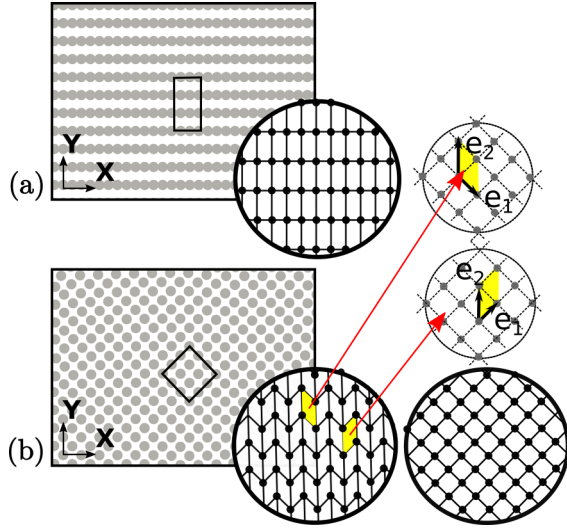
FIG. 9. A detail of the crystal structure deformed along the rectangular path, before and after the instability. The apparently rotated square lattice is obtained by a combination of microscopically compatible sheared configurations.

rotation at the macroscale is, in fact, a disguised microtwin mixture of the elements of the types $\mathbf{R}(\pi/2)\mathbf{S}_1^0$ and $\mathbf{S}_{-1}^0$. The zoom on the two configurations, before and after the instability, is shown in Fig. 9. It affirms that inside the rotated patch the (loaded) rectangular lattice is transformed into the (unloaded) square lattice which turns out to be a crystallographically exact mixture of microscopically compatible sheared square lattice configurations.

In Figs. 10 and 11, we show in more detail two representative fragments of the distorted network of our elastic elements illustrating two different types of interfaces between misaligned patches of the original lattice. The fragment, presented in Figs. 10(a), 10(b) and 10(c), details the rotation mechanism shown in Fig. 9 but now in the context of an actual decomposition pattern from Fig. 6. The observed microstructures can be predicted based on the macroscaopic strain compatibility requirement.

A. Geometric compatibility

Indeed, consider the deformation field $\mathbf{y}(\mathbf{x})$ whose deformation gradients $\mathbf{F} = \nabla\mathbf{y}_+$ and $\mathbf{G} = \nabla\mathbf{y}_-$ are discontinuous on the surface Σ. For the deformation itself to remain continuous on the surface Σ, the matrices $\mathbf{F}$, and $\mathbf{G}$ must be rank-one connected which constitutes the kinematic (Hadamard) compatibility condition

$$\mathbf{RF} = \mathbf{G} + \mathbf{a} \otimes \mathbf{n}^* = \mathbf{G}(\mathbf{I} + \mathbf{a}^* \otimes \mathbf{n}^*) = (\mathbf{I} + \mathbf{a} \otimes \mathbf{n})\mathbf{G}, \tag{10}$$

where $\mathbf{R} \in SO(2)$ is a rotation.

The Eulerian vector $\mathbf{n}$ (normal to the discontinuity plane) and covector $\mathbf{a}$, defining the amplitude of the shear, must satisfy $\mathbf{a} \cdot \mathbf{n} = 0$; their Lagrangian counterparts are $\mathbf{a}^* = \mathbf{G}^{-1}\mathbf{a}$ and $\mathbf{n}^* = \mathbf{G}^T\mathbf{n}$. If we assume further that $\det \mathbf{F} = \det \mathbf{G} = 1$ and exclude reflections, then the deformation gradients satisfying Eq. (10) form a mechanical twin. If, in addition, the rotation $\mathbf{R}$ belongs to the point group of the lattice, then such a twinning structure produces the undistorted zero energy configuration. The resulting microtwinned laminates are sometimes referred to as pseudotwins [77].

B. Twinning equation

Equation (10) was studied extensively; see, for instance, Refs. [123,124]. It was shown that Eq. (10) admits either no solutions or two solutions. More specifically, the two solutions exist when the matrix $\mathbf{G}^{-T}\mathbf{F}^T\mathbf{FG}^{-1} \neq \mathbf{I}$ and its ordered eigenvalues $\mu_1 < \mu_2$ are such that $\mu_1\mu_2 = 1$. In that case, the two solutions are given explicitly by the formulas

$$\mathbf{a} = \rho\left(\sqrt{\frac{\mu_2(1-\mu_1)}{\mu_2-\mu_1}}\mathbf{v}_1 + \kappa\sqrt{\frac{\mu_1(\mu_2-1)}{\mu_2-\mu_1}}\mathbf{v}_2\right), \tag{11}$$

$$\mathbf{n} = \frac{1}{\rho}\left(\frac{\sqrt{\mu_2}-\sqrt{\mu_1}}{\sqrt{\mu_2-\mu_1}}\right)(-\sqrt{1-\mu_1}\mathbf{v}_1 + \kappa\sqrt{\mu_2-1}\mathbf{v}_2), \tag{12}$$

where $\hat{\mathbf{v}}_1$ and $\hat{\mathbf{v}}_2$ are the normalized eigenvectors of $\mathbf{G}^{-T}\mathbf{F}^T\mathbf{FG}^{-1}$, $\rho > 0$ is a constant ensuring that $|\mathbf{n}| = 1$ and
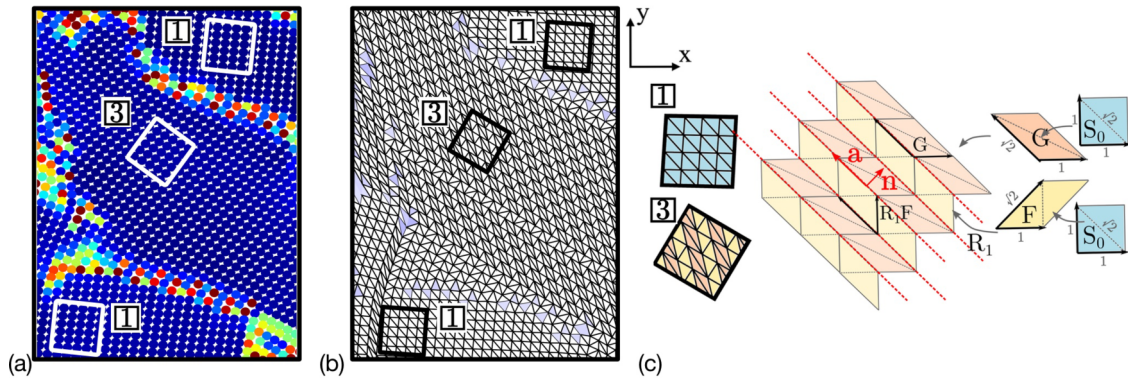

FIG. 10. A magnified fragment of the post-avalanche pattern from Fig. 6 showing the nodal coordinates in panel (a) and the actual affine distortions of individual finite elements in panel (b). The fragment is chosen to emphasize the coexistence of rotated patches of types 1 and 3 and the microtwin laminate structure of rotation in the patches of type 3. In panel (b) the finite element triangles are colored according to the level of their strain-energy but only when it is above a certain threshold: uncolored elements have very low energy; (c) illustration of the solution of the compatibility equation describing the laminate structure of the rotated patches of type 3.
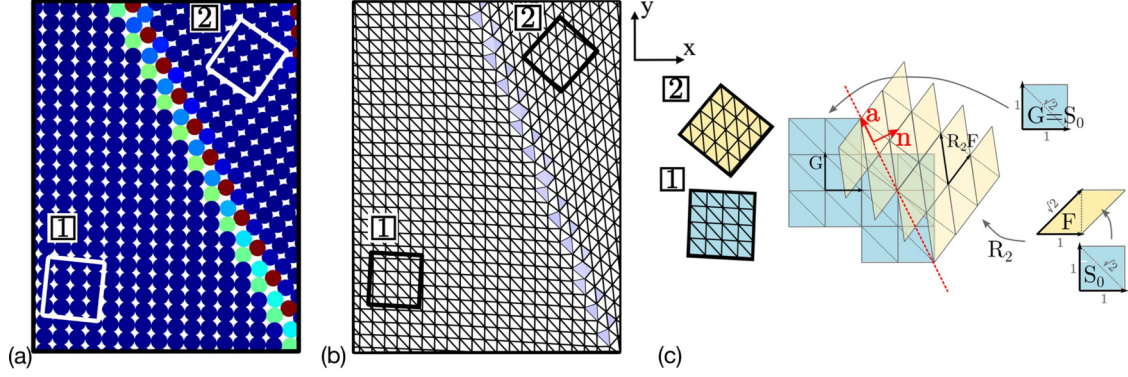
FIG. 11. A magnified fragment of the post-avalanche pattern from Fig. 6 showing the nodal coordinates in panel (a) and the actual affine distortions of individual finite elements in panel (b). The fragment is chosen to show the coexistence of patches of the type 1 and 2. Finite element triangles in panel (b) are colored according to the level of their strain-energy but only when it exceeds a certain threshold: uncolored traungles have low energy; (c) illustration of the corresponding solution of the compatibility equation.

$\kappa = \pm 1$. Once **a** and **n** are known, the rotation **R** can be obtained directly from Eq. (10).

Here, we are interested in the special case of compatibility between two $GL(2, \mathbb{Z})$ related deformation gradients, in other words, for the case when **G** and **F** are two equivalent minima of the strain-energy ϕ.

Consider first pseudotwins shown in Fig. 9 and Figs. 10(a) and 10(b), where **F** is in $\mathbf{S}_1^0$ and **G** is in $\mathbf{S}_{-1}^0$. For this case the condition $\mathbf{G}^{-T}\mathbf{F}^T\mathbf{F}\mathbf{G}^{-1} \neq \mathbf{I}$ is satisfied and the solution corresponding to $\kappa = 1$ is the one observed in our post-instability patchy pattern. It is characterized by the parameters $\mathbf{a}^T = \{-\sqrt{2}, \sqrt{2}\}$, $\mathbf{n}^T = \{\cos\zeta, \sin\zeta\}$, $\zeta = \pi/4$ with **R** a counter-clockwise rotation of $\psi = 2\zeta = \pi/2$, see our Figs. 10(c) and 12(a). For $\kappa = -1$, the solution is $\mathbf{a}^T = \{-2, 0\}$, $\mathbf{n}^T = \{\cos\zeta, \sin\zeta\}$, $\zeta = -\pi/2$ with $\mathbf{R}(\psi = 0)$. The corresponding microtwins, see Fig. 12(b), can be seen, for instance, in Fig. 10(b) in the bottom left "triangle" between the rotated patches of types 1 and 3. Note that such grain boundaries are neither microscopically nor macroscopically compatible as the corresponding habit planes do not exist in this system. The study of their dislocational structure will be presented separately. A more conventional case of misoriented coexisting patches of the original lattice (patches of types 1 and 2) is shown in Figs. 11(a) and 11(b). Here the deformation gradients **G** and **F** correspond to the bottoms of the energy wells $\mathbf{S}^0$ and $\mathbf{S}_1^0$, respectively. The two solutions of the twinning equation are: $\mathbf{a}^T = \{-\sin\zeta, \cos\zeta\}$, $\mathbf{n}^T = \{\cos\zeta, \sin\zeta\}$, $\mathbf{R}(\psi = 2\zeta)$, $\zeta = \arctan(1/2)$, for $\kappa = 1$, and $\mathbf{a}^T = \{1, 0\}$, $\mathbf{n}^T = \{\cos\zeta, \sin\zeta\}$, $\mathbf{R}(\psi = 0)$, $\zeta = -\pi/2$, for $\kappa = -1$. The so-

lution corresponding to $\kappa = 1$ was observed in our post-avalanche patchy pattern, see our Fig. 11(b), but not as a microscopically compatible microtwin laminate but, instead, as a macroscopically compatible but microscopically semi-coherent low-energy interface known as $\Sigma 5$ grain boundary [125]; see Figs. 11(c) and 13(a). The solution corresponding to $\kappa = -1$, Fig. 13(b), was not observed as a macroscopic grain boundary even though the associated configuration was effectively developing each time a dislocation was crossing the crystal.

Note that despite the full stress relaxation inside the two types of rotated patches shown in Figs. 10 and 11, the associated rotations are neither elastic nor rigid. Instead, they are achieved through distributed crystallographically exact shear. They are therefore slip-induced and fully dissipative, see also Ref. [126] for related experimental observations. In the next section, we elucidate the mechanism of such inelastic rotations by simulating analogous phenomena in the specially designed prototypical models.

V. PROTOTYPICAL MODELS

To accentuate the mechanism of "rotation by microtwinning," shown Figs. 10(a) and 10(b), we consider below a prototypical energy density, specially designed to ensure that only one slip mechanism, involving the energy wells $\mathbf{S}_1^0$ and $\mathbf{S}_{-1}^0$, is activated.
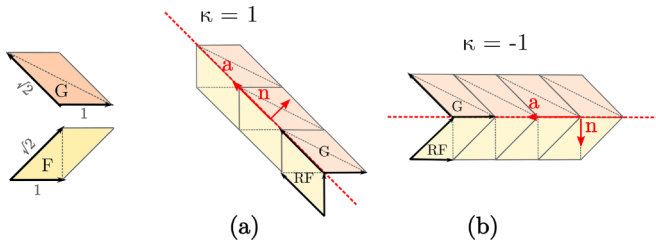

FIG. 12. The two solutions of the twinning equation (10) for the deformation gradients $\mathbf{F} = \mathbf{S}_1^0$ and $\mathbf{G} = \mathbf{S}_{-1}^0$.
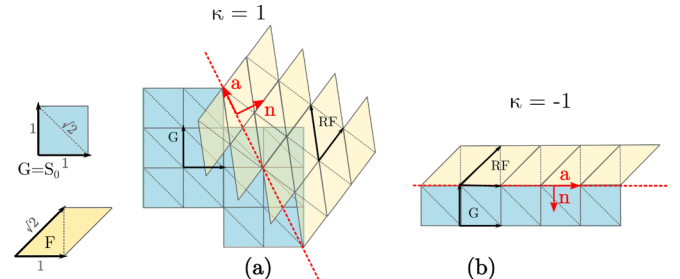

FIG. 13. The two solutions of the twinning equation (10) for the deformation gradients $\mathbf{F} = \mathbf{S}_1^0$ and $\mathbf{G} = \mathbf{S}^0 = \mathbf{I}$.
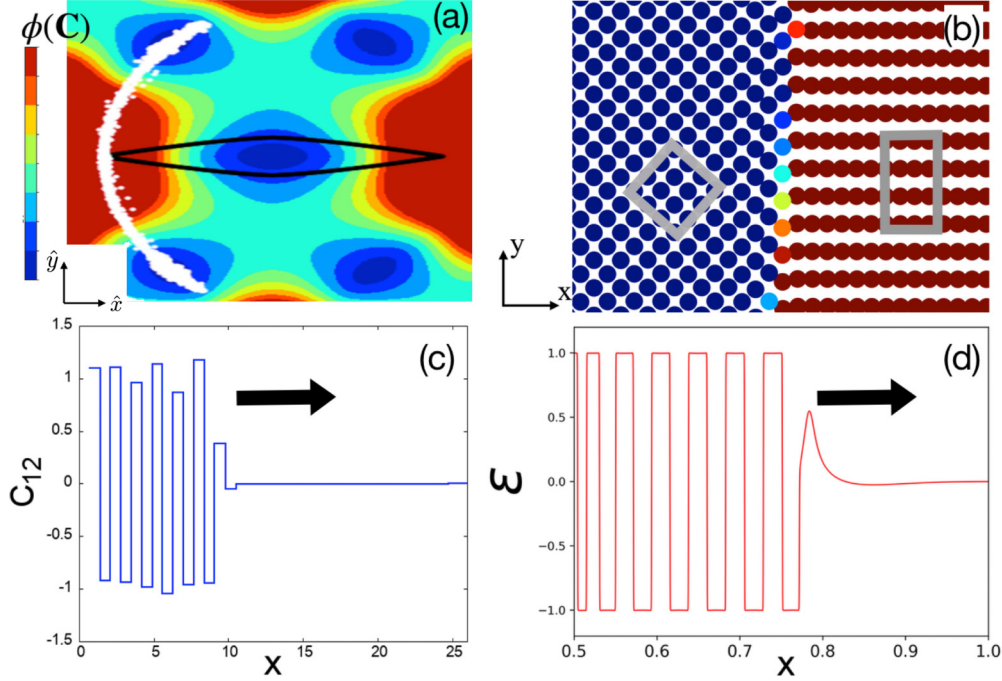
FIG. 14. The unfolding of the dislocation avalanche in the single-slip-biased version of the model. (a) Energy landscape showing the post-avalanche spreading of configurational points; (b) the structure of the moving front separating the initially stretched rectangular lattice and the growing microtwinned (rotated) square lattice (colors indicate the level of energy); (c) the distribution of the shear strain C_{12} across the transformation front shown in panel (b); (d) propagating front of lamination in the one dimensional toy model with parameters $\beta = 3 \times 10^{-6}$, $\eta = 0.0017$, $\gamma = 10^{-6}$, $A = -0.001$.

A. 2D prototypical model

The required bias can be achieved if, the volumetric distortions are strongly penalized. The prototypical energy density can be then taken in the additive form

$$\phi(\mathbf{C}) = \phi_v(\det \mathbf{C}) + \phi_s(\tilde{\mathbf{C}}), \tag{13}$$

where $\tilde{\mathbf{C}} = \mathbf{C}/(\det \mathbf{C})^{1/2}$. The volumetric part $\phi_v(s)$ will be chosen in the form $\mu[s - \log(s)]$ with stiff bulk modulus $\mu = 25$ which precludes (physically likely) softening in tension while still banning configurations with infinite compression.

The volume preserving shear energy ϕ_s needs to be specified only inside a single domain of periodicity and then extended by global symmetry. The convenient choice is the lowest-order polynomial which ensures the continuity of the elastic moduli [66]. A minimal expression of this type was proposed in Ref. [67] and we adopted it in our simulations. It has the form

$$\phi_s(\tilde{\mathbf{C}}) = \beta \psi_1(\tilde{\mathbf{C}}) + \psi_2(\tilde{\mathbf{C}}), \tag{14}$$

where $\psi_1 = I_1^4 I_2 - 41 I_2^3/99 + 7 I_1 I_2 I_3/66 + I_3^2/1056$ and $\psi_2 = 4 I_2^3/11 + I_1^3 I_3 - 8 I_1 I_2 I_3/11 + 17 I_3^2/528$. Here we used the (hexagonal) invariant functions of the (normalized) metric tensor: $I_1 = \frac{1}{3}(\tilde{C}_{11} + \tilde{C}_{22} - \tilde{C}_{12})$, $I_2 = \frac{1}{4}(\tilde{C}_{11} - \tilde{C}_{22})^2 + \frac{1}{12}(\tilde{C}_{11} + \tilde{C}_{22} - 4\tilde{C}_{12})^2$, and $I_3 = (\tilde{C}_{11} - \tilde{C}_{22})^2(\tilde{C}_{11} + \tilde{C}_{22} - 4\tilde{C}_{12}) - \frac{1}{9}(\tilde{C}_{11} + \tilde{C}_{22} - 4\tilde{C}_{12})^3$. The choice $\beta = -1/4$ enforces the square symmetry on the reference state.

In Fig. 14(a) we show that under our loading protocol such choice of the energy density indeed biases the system toward activating only one slip system. The important here is not the particular structure of the function ϕ_s, which is largely con-

trolled by the GL$(2, \mathbb{Z})$ symmetry, but rather the structure of the function ϕ_v which is responsible for the highly elongated shape of the apparent "yield surface"; see Fig. 14(a). With this configuration of the "yield surface," the loading in pure shear $\mathbf{F}_\parallel(\alpha)$, (which means moving left from the origin along the horizontal path on the Poincare disk) leads to the breakdown in the immediate vicinity of the energy wells $\mathbf{S}_1^0$ and $\mathbf{S}_{-1}^0$. In Fig. 14(b) we show that during the avalanche in such system, a transition front forms separating the (rectangular) stressed configuration $\mathbf{S}$ and the unstressed stable laminate involving the states $\mathbf{R}(\pi/2)\mathbf{S}_1^0$ and $\mathbf{S}_{-1}^0$. This laminate takes the form of an apparently rigid $\pi/4$ rotation which develops behind the propagating front.

The corresponding transient "computational dynamics" inside the avalanche is illustrated in a movie presented in the Supplemental Material [112]. More specifically, our movie S3 [112] shows the fast time evolution of the deformation field $\mathbf{y}(\mathbf{x})$ when we use in the numerical experiments the polynomial strain-energy density described above. Compared to what we saw in movies S1 and S2 [112], here we observe a much more organized evolution that remains effectively "laminar" throughout the whole avalanche. Once again the two fronts, separating affine and nonaffine dynamics, start to propagate from the vertical boundaries of the body, however, in this artificially designed model they remain stable and the fast time "computational flow" never develops any "vortices." Instead, we observe the fast side (transversal) motion of dislocations which is highly organized as it leaves behind a new homogeneous state. In other words, a nonaffine transient evolution results in an affine final configuration (modulo a single residual defect resulting from a computational noise). Since the

lattice scale microtwinning which is disguised here as rigid rotation is accomplished through the motion of dislocations, the resulting deformation is inelastic and the corresponding rotation should be qualified as dissipative.

B. One-dimensional prototypical model

An even more schematic, 1D prototypical description of the propagating transition front, imitating the one shown in Fig. 14(b), can be obtained if we neglect the transversal motion of dislocations and focus instead on the development of a laminate stabilized by competing interactions. To this end we need to introduce a scalar potential,

$$f(\epsilon) = (A/2)\epsilon^2 - (1/4)\epsilon^4 + (1/6)\epsilon^6, \qquad (15)$$

where $\epsilon = u_x$ and $u(x)$ is a scalar displacement field. The energy density (15) may have up to three wells with the higher-symmetry state playing the role of the deformed configuration **S**, and the two lower-symmetry states representing the symmetric variants $\mathbf{S}_1^0$ and $\mathbf{S}_{-1}^0$.

Consider next on the finite domain $0 \leqslant x \leqslant 1$ a continuum 1D system with the energy

$$E = \int_0^1 \left[f(u_x) + \frac{\beta}{2} u_{xx}^2 + \frac{\gamma}{2} u^2 \right] dx. \qquad (16)$$

Here the higher-order second term u_{xx}^2 represents the strain gradient regularization and brings an internal length scale. The lower order term u^2 represents the energy of the constraining elastic environment and also brings a (competing) length scale into the problem. Introducing the Rayleigh-type dissipation [127],

$$R = (\eta/2) \int_0^1 \dot{u}_x^2 dx, \qquad (17)$$

where η is the effective viscosity coefficient, we obtain the dynamic equation

$$\eta u_{xxt} = -f''(u_x)u_{xx} + \beta u_{xxxx} + \gamma u, \qquad (18)$$

whose role is to imitate the overdamped "computational dynamics" operative inside the duration of the avalanche.

To solve Eq. (18) numerically, we first approximate spatial derivatives by finite differences using a fixed grid with size Δh and utilize semi-implicit forward Euler discretization in time with a time step Δt. The resulting discrete set of equations in Fourier space takes the form

$$\hat{u}^{t+\Delta t}(q) = \frac{\eta \hat{M}_3(q)\hat{u}^t(q) - \Delta t \hat{M}_1(q)\hat{f}'(q)}{\eta \hat{M}_3(q) - dt(\beta \hat{M}_2(q) + \gamma)}, \qquad (19)$$

where $\hat{M}_1(q) = i\sin(q)/(2\Delta h)$, $\hat{M}_2(q) = 16\sin(q)^4/(\Delta h)^4$ and, $\hat{M}_3(q) = (2\cos(q) - 2)/(\Delta h)^2$. The discrete Fourier transform on a unit grid is defined as $\hat{u}(q) = N^{-1} \sum_i u_i e^{-iqx}$ with $x = i$ and $q = 2\pi k/N$, where $i = 0, 1, ..., N - 1$ and $k = 0, 1, ..., N - 1$. The nonlinear function $f' = \partial f/\partial u_x$ is

first evaluated in real space and then Fourier transformed to obtain $\hat{f}'(q)$. The Fourier image of the corresponding displacement field is computed as $\hat{u}(q) = \hat{\epsilon}(q)/\hat{M}_1(q)$ for $q \neq 0$. In our simulations, we used the parameter values: $\eta = 0.0017$, $\gamma = 10^{-6}$, $A = -10^{-3}$, $\beta = 3 \times 10^{-6}$, $\Delta h = 0.04$, $N = 8192$, and $\Delta t = 0.004$. The initial data were chosen in the form a localized strain increment $\epsilon(x) = 0.5e^{-(x-x_m)^2}$ centered around $x_m = 0.5$. Similar processes of growth of a stable microlaminate at the expense of an unstable homogeneous state have been studied before in many other settings [128–130].

The numerical solution of Eq. (18) is compared in Figs. 14(c) and 14(d) with the corresponding interavalanche dynamics in the single-slip prototypical version of our 2D model. The snapshots of the time evolution of the strain field $\epsilon(x, t)$ are shown in Fig. 15. The actual dynamic development of the microtwin pattern can be also followed in a movie presented in the Supplemental Material [112].

More specifically, our movie S4 [112] illustrates the dynamic growth of a laminate from a homogeneous state in front of it. One can see that the pattern formation emerges as an invasion process, in which a piecewise smooth inhomogeneous state, which is stable, takes over a marginally unstable homogeneous state. We observe that the initial perturbation first grows in amplitude and then spreads in a form of a spatially periodic pattern. The ensuing growth of a laminate appears macroscopically as a front, traveling with a constant velocity, and apparently winning over the growth of bulk modes. The comparison of the propagating patterns in Figs. 14(c) and 14(d) suggests that despite drastic simplifications, the 1D model captures the essential features of the corresponding dynamic process in 2D.

VI. PSEUDOTURBULENCE

We have seen that, in contrast to the intentionally oversimplified scenario described above, the actual 2D problem exhibits much higher complexity of the post-avalanche texture. The access in such a problem to a broad variety of low energy configurations, enabled by inelastic rotations, foments the development of imperfection-sensitive and therefore necessarily complex grain structure. The post-instability "fluidity" of the system, associated with the sudden dramatic "opening" of the energy landscape, makes the system-size plastic avalanche inherently unstable. However, the system remains under control of elastic interactions and the necessity to minimize elastic energy leads to self-organization. The latter is manifested by the development of long-range correlations [131,132].

To emphasize the intermittent nature of the evolution of the interavalanche deformation, we follow a similar analysis of the granular system [10], and generate a displacement field connecting the dislocation-free state "before" the avalanche and the dislocation-rich state "immediately after" the avalanche. More specifically, we compute the fluctuating part of the total nodal displacements $\mathbf{u}(\mathbf{x}) = \mathbf{y}(\mathbf{x}) - \mathbf{F}_{[]}(\alpha_c)\mathbf{x}$. It is shown in Fig. 16 with a zoom on two correlated turbulent-type "eddies."

Furthermore, in Fig. 17(a) we show the power spectral density (PSD) of the field $\mathbf{u}(\mathbf{x})$, illustrating the presence of
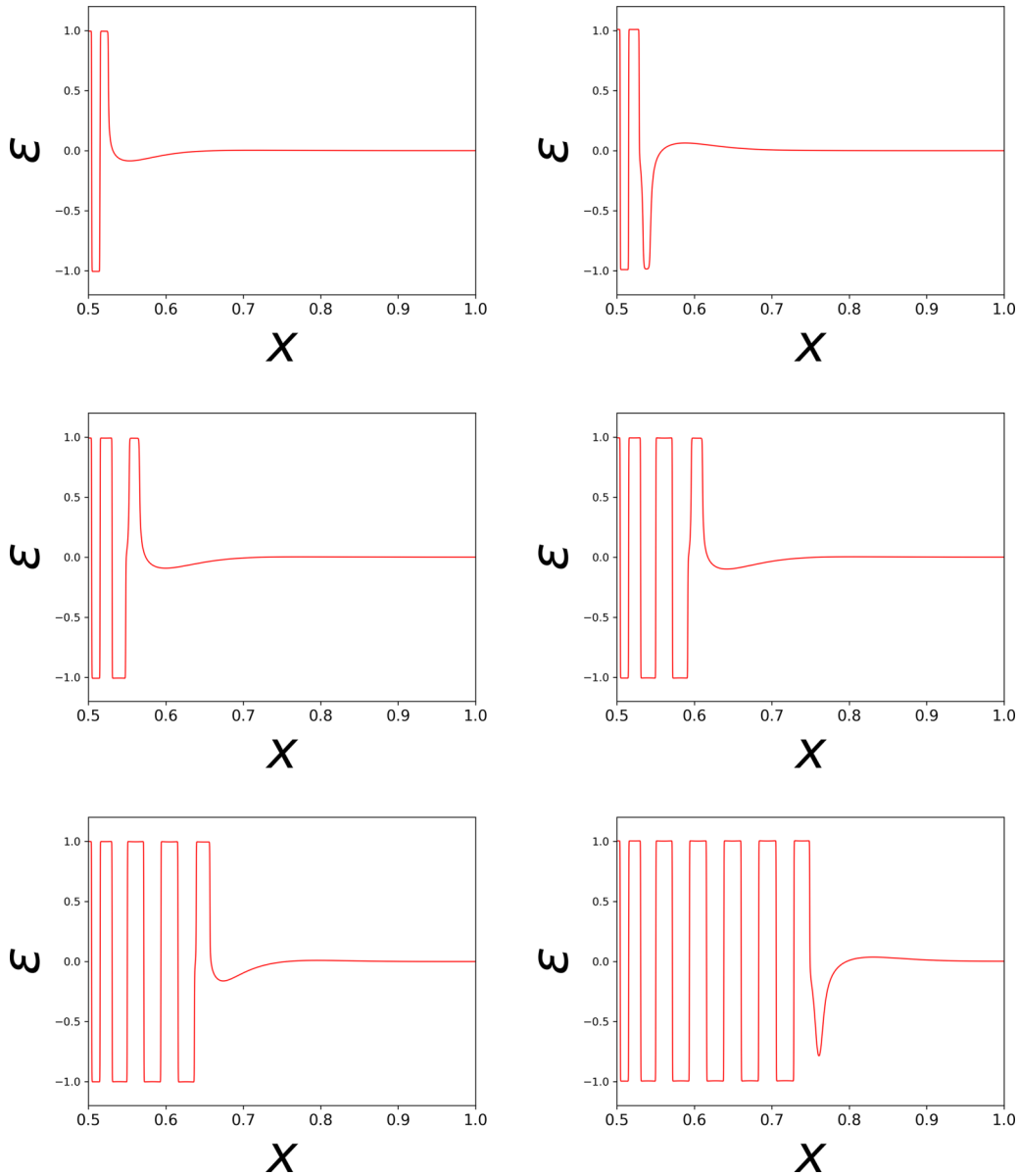
FIG. 15. Evolution of the strain field $\epsilon(x)$ at times $t = 390, 480, 580, 760, 970, 1350 \times dt$. The system ultimately evolves to the fully transformed state, which is a mixture of $\epsilon(x) \approx \pm 1$.

a hierarchy of scales and revealing the collective nature of the implied self-organization process. We recall that the PSD of a field $u(\mathbf{r})$ is a Fourier transform of the correlation function, $C(\mathbf{q}) = \mathcal{F}[\int u(\mathbf{r}_0)u(\mathbf{r}_0 + \mathbf{r})d\mathbf{r}_0]$ and since it depends on wave number and orientation, we performed the radial averaging over orientations to obtain the function $C(q)$, with $q = |\mathbf{q}|$, shown Fig. 17(a).

Observe that outside the small wave-number threshold this function exhibits a power law asymptotics $C(q)/q \sim q^{-2H-2}$. Our model produced the noninteger values for the Hurst exponent $H \approx 0.75$ and for the fractal dimension $D = 3 - H \approx 2.25$, independently of the choice of the component. Such scaling indicates the self-affine (rough) nature of the surfaces representing the displacement field and is indicative of hierarchical organization [133–136]. Moreover, similar to what is known about fluid turbulence, our Fig. 17(b) also shows

that the probability distribution function for at least one of the displacement derivatives is also characterized by robust algebraic tails.

Based on these observations, one can argue that the spatial correlations displayed by our MTM-based numerical tests display scaling characteristics that are indicative of turbulent-type dynamic rearrangements. Temporal correlations, associated with plastic yield, are also known to be of self-affine nature and to exhibit power-law correlations as they were captured by even the simplest scalar version of the MTM [6,58]. Similar analogies with fluid turbulence have been drawn in the analysis of several other complex disordered systems with domineering long-range interactions that are subjected to quasistatic driving, from brittle cracking to active evolution of tissues [137–142]. In particular, simulations and experiments recording plastic avalanches in a collection
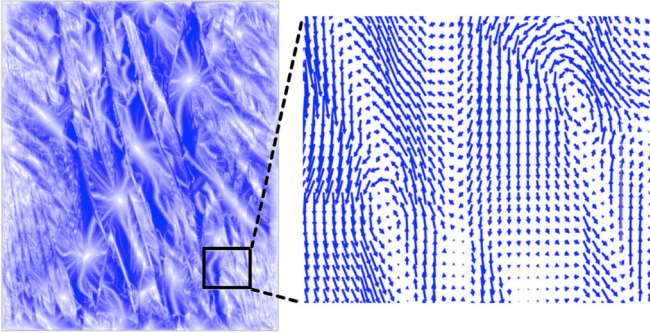
FIG. 16. Pseudoturbulent structure of the deformation field resulting from a dislocation avalanche. The displacement vectors connect pre- and post-avalanche positions of the individual nodes.

of sheared granular particles reveal nonaffine displacement fields exhibiting the probability distribution functions with much wider tails than Gaussian [10,114,115,117,143,144]. For related observations in crystal plasticity simulations involving experiments and non-MTM modeling techniques, see Refs. [142,145–148].

One may question the analogy between plastic avalanches and fluid turbulence based on the fact that in the former case we compare two static states, "before" and "after" the instability, while in the latter, the motion is continuous both in space and in time. Moreover in fluid turbulence the emerging scale invariance is related to a balance between the energy that is continuously injected at large length scales and removed at small length scales while in plastic avalanches such energy cascades are not apparent.

To substantiate the analogy, however, it is helpful to interpret a plastic avalanche as a dynamic process that converts the potential energy accumulated in the metastable state "before," into either acoustic radiation or heat, as the system transforms into a stable state "after." Such a transformation process starts

indeed from a static configuration but then it reaches a dynamic stage. As the initially stored energy is exhausted, the dynamics itself experiences a decay, so eventually the system reaches a new static configuration. In this picture, the dynamic stage is clearly present, as well the energy cascade from large scales (stored elastic energy) to small scales (acoustic radiation and heat). Although the associated dynamic process is not inertial, as in fluid turbulence, it can still generate self-induced complexity due to severe nonlinearity and the dominance of long-range interactions.

It is interesting that, while the physical nature of the "pseudoturbulence" in our overdamped solid system is clearly different from the classical inertial turbulence in fluids, the complexity-generating nonlinearity may be similarly *geometric*, meaning *universal*. Thus, the first source of nonlinearity in MTM is simply quadratic, as it is associated with the necessity to use finite strains in the description of deformations. This type of geometric nonlinearity is unavoidable if one wishes to capture correctly large crystal rotations [149–151]. While the second source of nonlinearity is of constitutive nature (multiwell Landau potential), it can be also considered as geometric. Indeed, it is related to the geometrical location of the energy wells which is fully controlled by the structure of lattice invariant shears. The energy wells themselves can be simply parabolic as we have previously shown using the scalar version of the MTM [58,152]. Moreover, similar to the case of high Reynolds fluid turbulence, the evolution generated by MTM is fully conservative outside intermittent avalanches. Furthermore, due to the quasistatic nature of the loading, the avalanches themselves remain dissipative even as the microscopic viscosity (encapsulated in numerical energy minimization) tends to zero [69]. Finally, as in fluid turbulence, the governing equations of the MTM become scale-free in the limit when the cut-off length tends to zero which ultimately explains the emergence of scale-free behavior.
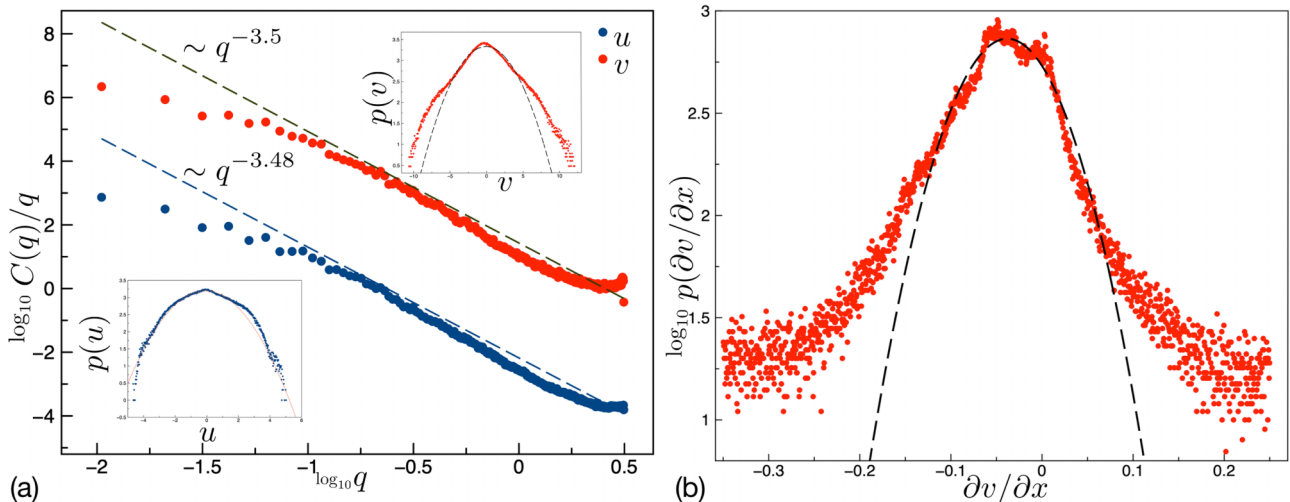

FIG. 17. (a) Fourier transform of auto-correlation function (power spectrum density) of the horizontal u and vertical v components of the displacement field; we interpret both components as surfaces which due to averaging are transitionally invariant and isotropic; the dashed lines show the power-law fit; insets show probability distributions $p(u)$ and $p(v)$. (b) Probability distribution $p(\partial v/\partial x)$ of the horizontal derivative of the displacement field exhibiting non-Gaussian wide tails.

VII. CONCLUSIONS

Plastic deformations in crystals originate from the availability of soft deformation modes which are usually represented as combinations of lattice-specific slips and rigid rotations. Above certain level of stress, elastic deformations are comperatively disfavored due to their high energetic cost. As a result, plastically deforming crystals typically form cell-based textures with elastic energy localized only on the boundaries separating randomly oriented patches or grains that are rotated relative to each other while being effectively unstressed.

In this paper, we used a mesoscopic tensorial model (MTM) to show that even large lattice rotations constituting such textures, can originate from a highly coordinated inelastic slip at the microscale. More specifically, we presented numerical evidence that behind such rotations may be crystallographically exact microslip laminates of a pseudotwin type.

The formation of such laminates can be viewed as an effective internal "wrinkling" of the crystal lattice and since a lattice independent internal scale is missing, the laminate microstructure forms at the scale of individual elastic elements. While the microlaminates disguise themselves as elastically neutral rotations, our numerical experiments reveal that the process of their formation is inherently dissipative. By studying the dynamic mechanisms leading to such rotations, we showed that they emerge from dislocation-mediated processes at the microscale.

The new insights were obtained due to the ability of the MTM approach to capture not only dislocation motion but also the dynamics of individual slips. An important finding revealed by our numerical experiments is that dislocation avalanches, resulting in the formation of rotated patches, involve pseudoturbulent rearrangements and lead to deformation fields exhibiting power-law distributed spatial correlations.

Being mesoscopic, the MTM approach is necessarily a result of coarse-graining of an atomistic model, but at a much finer scale than the classical continuum theory. Therefore, in MTM the fully nonlocal atom-by-atom interactions are inevitably lost and, for instance, dislocation core structures appear as blurred. However, as we have shown in our study, the MTM is capable to represent adequately not only the long-range but also the short-range interactions of dislocations which are essential for the description of dislocation nucleation and annihilation as well as the formation of their stable interlocked configurations.

The MTM approach should be developed further to address some puzzling problems in materials science and crystal physics. One of them is to rationalize the size dependence of the mechanical response of submicron structural elements, in particular, to explain their enhanced strength, the erratic nature of their stress-strain curves, and their propensity to discontinuous yield and brittle failure. A related challenge is to move from the study of single avalanches to numerical experiments addressing temporal intermittency in steady plastic flows. The goal here is to obtain fundamental insights into the origin of scale-free correlations in plastic fluctuations and to learn how to identify and interpret their statistical structure.

To simulate realistic crystalline structures, such as FCC, BCC, and HCP, it will be necessary to extend the MTM approach from 2D to 3D which should start with the construction of an appropriate $GL(3, \mathbb{Z})$-invariant energy. The 3D extension of MTM can be used to advance from basic modeling to actual engineering applications, in particular, for calibrating the augmented engineering continuum models accounting for microscopic effects [3]. In particular, such development will equip engineering models with the tools to adequately reproduce intermittent mechanical noise and will open them to the development of fluctuation-based nondestructive diagnostic techniques.

[1] M. Zaiser, P. Moretti, and H. Chu, Adv. Eng. Mater. **22**, 1901208 (2020).

[2] M. Ovaska, A. Lehtinen, M. J. Alava, L. Laurson, and S. Zapperi, Phys. Rev. Lett. **119**, 265501 (2017).

[3] J. Weiss, W. B. Rhouma, T. Richeton, S. Dechanel, F. Louchet, and L. Truskinovsky, Phys. Rev. Lett. **114**, 105504 (2015).

[4] I. Groma, in *Mesoscale Models: From Micro-Physics to Macro-Interpretation*, edited by S. Mesarovic, S. Forest, and H. Zbib (Springer International Publishing, Cham, 2019), pp. 87–139.

[5] S. Papanikolaou, Y. Cui, and N. Ghoniem, Modell. Simul. Mater. Sci. Eng. **26**, 013001 (2018).

[6] P. Zhang, O. U. Salman, J. Weiss, and L. Truskinovsky, Phys. Rev. E **102**, 023006 (2020).

[7] A. H. Cottrell, in *Dislocations in Solids*, edited by F. R. N. Nabarro and M. S. Duesbery (Elsevier, Amsterdam, 2002), vol. 11, pp. vii–xvii.

[8] W. Choi, Y. Chen, S. Papanikolaou, and J. Sethna, Comput. Sci. Eng. **14**, 33 (2012).

[9] J. P. Bouchaud, M. Mézard, and G. Parisi, Phys. Rev. E Stat. Phys. Plasmas Fluids Relat. Interdiscip. Topics **52**, 3656 (1995).

[10] F. Radjai and S. Roux, Phys. Rev. Lett. **89**, 064302 (2002).

[11] S. Odunuga, Y. Li, P. Krasnochtchekov, P. Bellon, and R. S. Averback, Phys. Rev. Lett. **95**, 045901 (2005).

[12] V. L. Berdichevsky, J. Mech. Phys. Solids **129**, 83 (2019).

[13] M. J. Marcinkowski, Phys. Stat. Sol. (b) **152**, 9 (1989).

[14] I. A. Kunin, Int. J. Theor. Phys. **29**, 1167 (1990).

[15] E. V. Shilko, Y. V. Grinyaev, M. V. Popov, V. L. Popov, and S. G. Psakhie, Phys. Rev. E **93**, 053005 (2016).

[16] J. S. Andrade, Jr, H. J. Herrmann, R. F. S. Andrade, and L. R. da Silva, Phys. Rev. Lett. **94**, 018702 (2005).

[17] R. Kulagin, Y. Beygelzimer, Y. Ivanisenko, A. Mazilkin, and H. Hahn, IOP Conf. Ser.: Mater. Sci. Eng. **194**, 012045 (2017).

[18] J. Oddershede, J. P. Wright, A. Beaudoin, and G. Winther, Acta Mater. **85**, 301 (2015).

[19] S. Hémery and P. Villechaise, Acta Mater. **171**, 261 (2019).

[20] J. P. Sethna, V. R. Coffman, and E. Demler, Phys. Rev. B **67**, 184107 (2003).

[21] G. Winther, Mater. Sci. Eng.: A **483-484**, 40 (2008).

[22] F. P. E. Dunne, R. Kiwanuka, and A. J. Wilkinson, Proc. Math. Phys. Eng. Sci. **468**, 2509 (2012).

[23] G. M. Castelluccio and D. L. McDowell, Int. J. Plast. **98**, 1 (2017).

[24] A. Vinogradov and Y. Estrin, Prog. Mater. Sci. **95**, 172 (2018).

[25] R. Arora and A. Acharya, Int. J. Solids Struct. **184**, 114 (2020).

[26] R. J. Asaro, in *Advances in Applied Mechanics*, edited by J. W. Hutchinson and T. Y. Wu (Elsevier, Amsterdam, 1983), vol. 23, pp. 1–115.

[27] R. J. Asaro and A. Needleman, Acta Metall. **33**, 923 (1985).

[28] J. F. Besseling and E. Van Der Giessen, *Mathematical Modeling of Inelastic Deformation* (CRC Press, Boca Raton, FL, 1994).

[29] J. N. Florando, M. Rhee, A. Arsenlis, M. M. LeBlanc, and D. H. Lassila, Philos. Mag. Lett. **86**, 795 (2006).

[30] P. Chen, S. C. Mao, Y. Liu, F. Wang, Y. F. Zhang, Z. Zhang, and X. D. Han, Mater. Sci. Eng.: A **580**, 114 (2013).

[31] E. Van der Giessen, Int. J. Plast. **7**, 365 (1991).

[32] Y. F. Dafalias and E. C. Aifantis, Acta Mech. **82**, 31 (1990).

[33] K. Wierzbanowski, M. Wroński, A. Baczmański, B. Bacroix, P. Lipinski, and A. Lodini, Arch. Metall. Mater. **56**, 575 (2011).

[34] L. A. Zepeda-Ruiz, A. Stukowski, T. Oppelstrup, and V. V. Bulatov, Nature (London) **550**, 492 (2017).

[35] A. V. Korchuganov, A. N. Tyumentsev, K. P. Zolnikov, I. Y. Litovchenko, D. S. Kryzhevich, E. Gutmanas, S. Li, Z. Wang, and S. G. Psakhie, J. Mater. Sci. Technol. **35**, 201 (2019).

[36] W.-S. Ko, A. Stukowski, R. Hadian, A. Nematollahi, J. B. Jeon, W. S. Choi, G. Dehm, J. Neugebauer, C. Kirchlechner, and B. Grabowski, Acta Mater. **197**, 54 (2020).

[37] N. Bertin, R. B. Sills, and W. Cai, Annu. Rev. Mater. Res. **50**, 437 (2020).

[38] J. Wang, A. H. M. Faisal, X. Li, Y. Hong, Q. Zhu, H. Bei, Z. Zhang, S. X. Mao, and C. R. Weinberger, J. Mater. Sci. Technol. **106**, 33 (2022).

[39] D. Barba, E. Alabort, S. Pedrazzini, D. M. Collins, A. J. Wilkinson, P. A. J. Bagot, M. P. Moody, C. Atkinson, A. Jérusalem, and R. C. Reed, Acta Mater. **135**, 314 (2017).

[40] J. Zhai, Z. Yan, and H. Yu, Nanoscale Adv. **4**, 3711 (2022).

[41] A. Arsenlis, W. Cai, M. Tang, M. Rhee, T. Oppelstrup, G. Hommes, T. G. Pierce, and V. V. Bulatov, Modell. Simul. Mater. Sci. Eng. **15**, 553 (2007).

[42] C. Baruffi, A. Finel, Y. Le Bouar, B. Bacroix, and O. U. Salman, Mater. Theory **3**, 4 (2019).

[43] L. A. Zepeda-Ruiz, A. Stukowski, T. Oppelstrup, N. Bertin, N. R. Barton, R. Freitas, and V. V. Bulatov, Nat. Mater. **20**, 315 (2021).

[44] M. Salvalaglio, L. Angheluta, Z.-F. Huang, A. Voigt, K. R. Elder, and J. Viñals, J. Mech. Phys. Solids **137**, 103856 (2020).

[45] P. Y. Chan, G. Tsekenis, J. Dantzig, K. A. Dahmen, and N. Goldenfeld, Phys. Rev. Lett. **105**, 015502 (2010).

[46] B. Devincre, T. Hoc, and L. Kubin, Science **320**, 1745 (2008).

[47] P. D. Ispánovity, L. Laurson, M. Zaiser, I. Groma, S. Zapperi, and M. J. Alava, Phys. Rev. Lett. **112**, 235501 (2014).

[48] D. Gómez-García, B. Devincre, and L. P. Kubin, Phys. Rev. Lett. **96**, 125503 (2006).

[49] W. Cai, A. Arsenlis, C. R. Weinberger, and V. V. Bulatov, J. Mech. Phys. Solids **54**, 561 (2006).

[50] K. Starkey, G. Winther, and A. El-Azab, J. Mech. Phys. Solids **139**, 103926 (2020).

[51] M. Monavari, S. Sandfeld, and M. Zaiser, J. Mech. Phys. Solids **95**, 575 (2016).

[52] P. Lin, V. Vivekanandan, K. Starkey, B. Anglin, C. Geller, and A. El-Azab, Int. J. Plast. **138**, 102943 (2021).

[53] I. Groma, P. D. Ispánovity, and T. Hochrainer, Phys. Rev. B **103**, 174101 (2021).

[54] V. B. Shenoy, R. Miller, E. b. Tadmor, D. Rodney, R. Phillips, and M. Ortiz, J. Mech. Phys. Solids **47**, 611 (1999).

[55] M. Javanbakht and V. I. Levitas, Int. J. Solids Struct. **82**, 95 (2016).

[56] N. Bruzy, C. Denoual, and A. Vattré, J. Mech. Phys. Solids **166**, 104921 (2022).

[57] P. Biscari, M. F. Urbano, A. Zanzottera, and G. Zanzotto, J. Elast. **123**, 85 (2016).

[58] O. U. Salman and L. Truskinovsky, Phys. Rev. Lett. **106**, 175503 (2011).

[59] R. Baggio, E. Arbib, P. Biscari, S. Conti, L. Truskinovsky, G. Zanzotto, and O. U. Salman, Phys. Rev. Lett. **123**, 205501 (2019).

[60] J. L. Ericksen, Arch. Ration. Mech. Anal. **73**, 99 (1980).

[61] L. L. Boyer, Acta Crystallogr. A Found. Crystallogr. **45**, fc29 (1989).

[62] I. Folkins, J. Math. Phys. **32**, 1965 (1991).

[63] J. Wang, S. Yip, S. R. Phillpot, and D. Wolf, Phys. Rev. Lett. **71**, 4182 (1993).

[64] B. W. Waal, Acta Crystallogr. A Found. Crystallogr. **46**, 17 (1990).

[65] E. Kaxiras and L. L. Boyer, Phys. Rev. B **50**, 1535 (1994).

[66] G. P. Parry, Arch. Ration. Mech. Anal. **145**, 1 (1998).

[67] S. Conti and G. Zanzotto, Arch. Ration. Mech. Anal. **173**, 69 (2004).

[68] O. U. Salman, R. Baggio, B. Bacroix, G. Zanzotto, N. Gorbushin, and L. Truskinovsky, C. R. Phys. **22**, 1 (2021).

[69] G. Puglisi and L. Truskinovsky, J. Mech. Phys. Solids **53**, 655 (2005).

[70] E. B. Tadmor, M. Ortiz, and R. Phillips, Philos. Mag. A **73**, 1529 (1996).

[71] J. Li, T. Zhu, S. Yip, K. J. Van Vliet, and S. Suresh, Mater. Sci. Eng.: A **365**, 25 (2004).

[72] R. L. Hayes, M. Fago, M. Ortiz, and E. A. Carter, Multiscale Model. Simul. **4**, 359 (2005).

[73] D. Rodney, Y. Le Bouar, and A. Finel, Acta Mater. **51**, 17 (2003).

[74] V. I. Levitas and M. Javanbakht, Phys. Rev. B **86**, 140101(R) (2012).

[75] C. Denoual and A. Vattré, J. Mech. Phys. Solids **90**, 91 (2016).

[76] X. Hu, Y. Ji, L. Chen, R. A. Lebensohn, L.-Q. Chen, and X. Cui, Int. J. Plast. **143**, 103019 (2021).

[77] M. Pitteri and G. Zanzotto, *Continuum Models for Phase Transitions and Twinning in Crystals* (Chapman and Hall/CRC, Boca Raton, FL, 2002).

[78] R. Peierls, Proc. Phys. Soc. **52**, 34 (1940).

[79] F. R. N. Nabarro, Proc. Phys. Soc. **59**, 256 (1947).

[80] J. Frenkel and T. Kontorova, Izv. Akad. Nauk, Ser. Fiz. **1**, 137 (1939).

[81] M. Ortiz and E. A. Repetto, J. Mech. Phys. Solids **47**, 397 (1999).

[82] S. Conti, G. Dolzmann, and C. Kreisbeck, in *Analysis and Computation of Microstructure in Finite Plasticity*, edited by S. Conti and K. Hackl (Springer International Publishing, Cham, 2015), pp. 31–62.

[83] M. Pitteri, J. Elast. **14**, 175 (1984).

[84] B. D. Coleman and W. Noll, Arch. Ration. Mech. Anal. **15**, 87 (1964).

[85] C. Truesdell and W. Noll, in *The Non-Linear Field Theories of Mechanics*, edited by C. Truesdell, W. Noll, and S. S. Antman (Springer, Berlin, 2004), pp. 1–579.

[86] P. Engel, *Geometric Crystallography: An Axiomatic Introduction to Crystallography* (Springer, Netherlands, 1986).

[87] L. L. Boyer, Phys. Rev. B **53**, 3145 (1996).

[88] Y. Gao, Y. Wang, and Y. Zhang, IUCrJ **6**, 96 (2019).

[89] A. Minami and A. Onuki, Acta Mater. **55**, 2375 (2007).

[90] A. Onuki, Phys. Rev. E **68**, 061502 (2003).

[91] A. Carpio and L. L. Bonilla, Phys. Rev. B **71**, 134105 (2005).

[92] P.-A. Geslin, B. Appolaire, and A. Finel, Acta Mater. **71**, 80 (2014).

[93] J. L. Ericksen, Math. Mech. Solids **13**, 199 (2008).

[94] Y.-M. Juan and E. Kaxiras, J. Comput.-Aided Mater. Des. **1**, 55 (1993).

[95] R. Sunyk and P. Steinmann, Int. J. Solids Struct. **40**, 6877 (2003).

[96] A. Marano, L. Gélébart, and S. Forest, Acta Mater. **175**, 262 (2019).

[97] M. Destrade, J. G. Murphy, and G. Saccomandi, Int. J. Non Linear Mech. **47**, 210 (2012).

[98] S. Bochkanov and V. Bystritsky, Available from: www.alglib.net (2013).

[99] I. Fonseca, Arch. Ration. Mech. Anal. **97**, 189 (1987).

[100] A. Arsenlis and D. M. Parks, Acta Mater. **47**, 1597 (1999).

[101] O. Rezvanian, M. A. Zikry, and A. M. Rajendran, Proc. R. Soc. London A **463**, 2833 (2007).

[102] K. Nguyen, M. Zhang, V. J. Amores, M. A. Sanz, and F. J. Montáns, Crystals **11**, 42 (2021).

[103] J. R. Rice, in *Proc. of the 14th IUTAM Congress* (North-Holland, Amsterdam, Netherlands, 1976), pp. 207–220.

[104] R. W. Ogden, *Non-linear Elastic Deformations* (Ellis Horwood, Chichester, 1984) (1997).

[105] D. Bigoni, *Nonlinear Solid Mechanics: Bifurcation Theory and Material Instability* (Cambridge University Press, Cambridge, UK, 2012).

[106] K. J. Van Vliet, J. Li, T. Zhu, S. Yip, and S. Suresh, Phys. Rev. B **67**, 104105 (2003).

[107] Y. Zhong and T. Zhu, Comput. Methods Appl. Mech. Eng. **197**, 3174 (2008).

[108] Y. Grabovsky and L. Truskinovsky, J. Nonlin. Sci. **23**, 891 (2013).

[109] R. E. Miller and D. Rodney, J. Mech. Phys. Solids **56**, 1203 (2008).

[110] A. Garg and C. E. Maloney, J. Mech. Phys. Solids **95**, 742 (2016).

[111] D. L. Medlin, N. Yang, C. D. Spataru, L. M. Hale, and Y. Mishin, Nat. Commun. **10**, 1 (2019).

[112] See Supplemental Material at http://link.aps.org/supplemental/10.1103/PhysRevE.107.025004 for illustrative movies.

[113] A. Misra and H. Jiang, Comput. Geotech. **20**, 267 (1997).

[114] G. Combe, V. Richefeu, G. Viggiani, S. A. Hall, A. Tengattini, and A. P. F. Atman, in *in Powders and Grains 2013: Proceedings of the 7th International Conference on Micromechanics of Granular Media* (AIP, Sydney, Australia, 2013).

[115] N. Oyama, H. Mizuno, and K. Saitoh, Phys. Rev. Lett. **122**, 188004 (2019).

[116] A. Sun, Y. Wang, Y. Chen, J. Shang, J. Zheng, S. Yu, S. Su, X. Sun, and J. Zhang, Soft Matter **18**, 983 (2022).

[117] C. Goldenberg, A. Tanguy, and J.-L. Barrat, Europhys. Lett. **80**, 16003 (2007).

[118] C. Ruscher and J. Rottler, J. Stat. Mech. **2019**, 093303 (2019).

[119] S. Cui, H. Liu, and H. Peng, Phys. Rev. E **106**, 014607 (2022).

[120] A. Stukowski, V. V. Bulatov, and A. Arsenlis, Modell. Simul. Mater. Sci. Eng. **20**, 085007 (2012).

[121] M. Elsey and B. Wirth, Multiscale Model. Simul. **12**, 1 (2014).

[122] C. D. Barrett, Philos. Mag. **97**, 1102 (2017).

[123] J. M. Ball and R. D. James, in *Analysis and Continuum Mechanics: A Collection of Papers Dedicated to J. Serrin on His Sixtieth Birthday*, edited by S. S. Antman, H. Brezis, B. D. Coleman, M. Feinberg, J. A. Nohel, and W. P. Ziemer (Springer, Berlin, 1989), pp. 647–686.

[124] A. Forclaz, J. Elast. **57**, 281 (1999).

[125] Y. Gao, Materialia **9**, 100588 (2020).

[126] I. A. Ovid'ko and A. G. Sheinerman, Appl. Phys. Lett. **98**, 181909 (2011).

[127] T. Lookman, S. R. Shenoy, K. Ø. Rasmussen, A. Saxena, and A. R. Bishop, Phys. Rev. B **67**, 024114 (2003).

[128] W. van Saarloos, Phys. Rep. **386**, 29 (2003).

[129] X. Ren and L. Truskinovsky, J. Elast. **59**, 319 (2000).

[130] A. Doelman, *The Dynamics of Modulated Wave Trains* (American Mathematical Society, Providence, RI, 2009).

[131] S. Gelin, H. Tanaka, and A. Lemaître, Nat. Mater. **15**, 1177 (2016).

[132] P.-A. Geslin, A. Rida, and D. Rodney, J. Mech. Phys. Solids **153**, 104480 (2021).

[133] K. R. Sreenivasan, Annu. Rev. Fluid Mech. **23**, 539 (1991).

[134] T. Y. Hou, X.-H. Wu, S. Chen, and Y. Zhou, Phys. Rev. E **58**, 5841 (1998).

[135] B. N. J. Persson, O. Albohr, U. Tartaglino, A. I. Volokitin, and E. Tosatti, J. Phys.: Condens. Matter **17**, R1 (2005).

[136] C. Türk, A. Carbone, and B. M. Chiaia, Phys. Rev. E **81**, 026706 (2010).

[137] A. V. Perig, A. M. Laptev, N. N. Golodenko, Y. A. Erfort, and E. A. Bondarenko, Mater. Sci. Eng.: A **527**, 3769 (2010).

[138] L. Angheluta, P. Jeraldo, K. Dahmen, and N. Goldenfeld, arXiv preprint arXiv:1103.2185 (2011).

[139] H. Borja da Rocha and L. Truskinovsky, Phys. Rev. Lett. **124**, 015501 (2020).

[140] S. Biswas and B. K. Chakrabarti, Phys. Rev. E **102**, 012113 (2020).

[141] R. Mandal, P. J. Bhuyan, P. Chaudhuri, C. Dasgupta, and M. Rao, Nat. Commun. **11**, 1 (2020).

[142] Y. Beygelzimer, A. E. Filippov, R. Kulagin, and Y. Estrin, arXiv:2111.05148 (2021).

[143] V. Richefeu, G. Combe, and G. Viggiani, Géotech. Lett. **2**, 113 (2012).

[144] T. Miller, P. Rognon, B. Metzger, and I. Einav, Phys. Rev. Lett. **111**, 058002 (2013).

[145] C. Fressengeas, A. J. Beaudoin, D. Entemeyer, T. Lebedkina, M. Lebyodkin, and V. Taupin, Phys. Rev. B **79**, 014108 (2009).

[146] J. Chevy, C. Fressengeas, M. Lebyodkin, V. Taupin, P. Bastie, and P. Duval, Acta Mater. **58**, 1837 (2010).

[147] L. Angheluta, P. Jeraldo, and N. Goldenfeld, Phys. Rev. E **85**, 011153 (2012).

[148] M. J. Alava, L. Laurson, and S. Zapperi, Eur. Phys. J. Spec. Top. **223**, 2353 (2014).

[149] Y. Grabovsky and L. Truskinovsky, Continuum Mech. Thermodyn. **19**, 211 (2007).

[150] A. Finel, Y. Le Bouar, A. Gaubert, and U. Salman, C. R. Phys. **11**, 245 (2010).

[151] O. U. Salman, B. Muite, and A. Finel, Eur. Phys. J. B **92**, 20 (2019).

[152] O. U. Salman and L. Truskinovsky, Int. J. Eng. Sci. **59**, 219 (2012).